NTNU

Norwegian University of
Science and Technology

# Amino-Functionalized Magnetic Nanoparticles for Extraction of Naphthenic Acids

Mikael Strand

Chemical Engineering and Biotechnology
Submission date: September 2016
Supervisor: Johan Sjöblom, IKP
Co-supervisor: Galina Rodionova, IKP

Norwegian University of Science and Technology
Department of Chemical Engineering

## Preface

This thesis concludes my Master of Science degree at the Department of Chemical Engineering of the Norwegian University of Science and Technology (NTNU). This project is based on a specialization project from the fall of 2015, and experimental work carried out at Ugelstad Laboratory in the first eight months of 2016. The experimental work was performed under the supervision of Professor Johan Sjöblom (main supervisor) and Dr. Galina Rodionova (co-supervisor).

I would like to thank Dr. Galina Rodionova, my co-supervisor, for all the help she has given me. Without her guidance and support, I would never have finished my thesis. I want to thank Dr. Sebastian Simon for always helping me whenever I may have had any questions. I am grateful to my main supervisor Professor Johan Sjöblom for giving me the opportunity to write this thesis.

I am also thankful to Dr. Jens Norrman for helping me with my QCM experiments and the analysis of the results and May Grete Sætran, Bicheng Gao and Camilla Israelsen Dagsgård for helping me whenever I had laboratory related questions. I am thankful to Ragnhild Sæterli for helping me with TEM imaging and the analysis of the results.

I declare that this is an independent work according to the exam regulations of the Norwegian University of Science and Technology (NTNU).

## Abstract

The present work is a part of a 2-year Post Doc project carried out by a Vista program funded by Statoil and conducted in close collaboration with The Norwegian Academy of Science and Letters. The goal of the main project is to establish new methods for both preventing formation and facilitating removal of naphthenic acids (NA). The newly developed methods will be based on the application of functionalized magnetic nanoparticles (FMN) for extraction of NA before formation of the metal naphthenates as well as their removal to avoid deposit formation.

The current Master's thesis is aiming for synthesis of magnetic naked ($Fe_3O_4$), silica-coated ($Fe_3O_4/SiO_2$) and amino-functionalized ($Fe_3O_4/SiO_2$ $NH_2/C_{18}$) nanoparticles, and their application for extraction of NA from a model oil.

As a first step, commercial silica particles with known amino group ($-NH_2$) grafting degree were purchased and tested to confirm the amino groups selectivity towards NA in a real crude oil. The oil used was an acidic sample from the Heidrun field in the North Sea. The total acid number (TAN) was measured before and after addition of the particles, and the result revealed a reduction of 92.2 % in crude oil acidity.

The $Fe_3O_4/SiO_2$ $NH_2/C_{18}$ nanoparticles were obtained through synthesis by two different methods, a high-pressure autoclave experiment with toluene as solvent and a reflux experiment using xylene as solvent, which has a higher boiling point. The particles were tested with respect to various parameters and exhibited magnetic properties. A specific surface area of 113 $m^2/g$ was measured for the $Fe_3O_4/SiO_2$ particles, while a reduction was registered for the functionalized samples. Elemental analysis revealed that 3-aminopropyltrimethoxysilane (APTMS) groups had been successfully grafted onto the surface, n-octadecyltriethoxysilane (ODS) had been grafted to a far lesser degree or not grafted at all. The electron microscopy revealed the magnetic core and silica coating of the separate particles as well as particle agglomerates. The average particle size and coating thickness were calculated based of a size distribution analysis. The two functionalization methods revealed similar results for the adsorption of model NA onto the particle surface. The amino-functionalized $Fe_3O_4/SiO_2$ $NH_2/C_{18}$ samples showed about 2.5 to 2.9 times higher adsorption capacity of 4-heptylbenzoic acid in octane compared to the silica-coated $Fe_3O_4/SiO_2$ particles from Master's thesis of Mia Ronader [1].

## Sammendrag

Dette arbeidet er en del av et 2-årig Post Doc prosjekt støttet av et Vista program. Dette programmet er finansielt støttet av Statoil og er gjennomført i nært samarbeid med Det Norske Videnskaps-Akademi. Hovedprosjektets mål er å etablerer nye metoder for å forhindre formasjoner av naftensyrer (NA) og for separere ut NA fra råolje. De nyutviklede metodene vil basere seg på bruk av funksjonaliserte magnetiserte nanopartikler (FMN) for ekstraksjon av NA før dannelse av metall naftenater.

Denne masteroppgaven retter seg mot syntetisering av magnetiske nakne ($Fe_3O_4$), silika-dekkede ($Fe_3O_4/SiO_2$) og aminofunksjonaliserte ($Fe_3O_4/SiO_2$ $NH_2/C_{18}$) nanopartikler, og deres evne til å ekstrahere ut NA fra en modell olje.

Kommersielle silikapartikler med kjent aminogruppeoverflatekonsentrasjon ($-NH_2$) ble kjøpt og testet for å bekrefte aminogruppens selektivitet mot NA i en ekte råolje. En sur råolje fra Heidrun feltet i Nordsjøen ble brukt. Det total syre tallet (TAN) ble målt før og etter tilsetting av partiklene, resultatene viste en reduksjon på 92.2% i råoljens TAN.

$Fe_3O_4/SiO_2$ $NH_2/C_{18}$ nanopartiklene ble syntetisert ved to forskjellige metoder, en med toluen som løsemiddel it en forseglet autoklav, og en i et refluks eksperiment med xylen som løsemiddel. Forskjellige parametere for partiklene ble testet og de viste magnetiske egenskaper. Et spesifikt overflateareal ble målt til 113 $m^2/g$ for $Fe_3O_4/SiO_2$ partiklene, det ble registrert en reduksjon for de funksjonaliserte partiklene. En element analyse viste at 3-aminopropyltremetoxysilane (APTMS) hadde festet seg på overflaten, n-oktadekyltrietoxysilane (ODS) hadde festet seg i mye mindre grad eller kanskje ikke i det heletatt. Elektronmikroskop viste partiklenes magnetiske kjerne og silikalaget som dekket kjernen, og en forklumpning av partiklene. Gjennomsnittlige partikkelstørrelsen og silika tykkelse ble funnet gjennom en størrelse distribusjons analyse. De to funksjonaliserings metodene viste lignende adsorpsjons egenskaper av NA på overflaten. De funksjonaliserte $Fe_3O_4/SiO_2$ $NH_2/C_{18}$ partiklene viste ca 2.5 til 2.9 ganger så stor adsorpsjonsegenskaper sammenlignet med silika-dekkede $Fe_3O_4/SiO_2$ partikler fra Master oppgaven til Mia Ronander [1].

## List of abbreviations

| | |
|---|---|
| APTMS | 3-Aminopropyltrimethoxysilane |
| APTES | 3-Aminpropyltriethoxysilane |
| ARN | A class of high molecular weight tetra-acids |
| BET | Brunauer-Emmett-Teller method |
| CTAB | Hexadecyl trimethylammonium bromide |
| DDBSA | Dodecylbenzene sulfonic acid |
| FEG | Field emission gun |
| FMN | Functionalized magnetic nanoparticles |
| FTIR | Fourier transform infrared spectroscopy |
| HBA | 4-Heptylbenzoic acid |
| M-EC | Magnetic ethyl-cellulose-grafted nanoparticles |
| MNP | Magnetic nanoparticles |
| MPSS | Magnetic nanoparticles coated with porous silica |
| MSCK | Magnetic shell cross-linked knedel-like nanoparticles |
| NA | Naphthenic acids |
| O/W | Oil-in-water |
| ODS | n-Octadecyltriethoxysilane |
| PEC | Particle exchange capacity |
| QCM | Quartz crystal microbalance |
| SEM | Scanning electron microscopy |
| TAN | Total acid number |
| TBA | Tetrabutyl-ammonium hydroxide |
| TEM | Transmission electron microscopy |
| TEOS | Tetraethoxysilane |
| UV-vis | Ultraviolet-visible spectroscopy |
| VTES | Vinyltriethoxysilane |
| W/O | Water-in-oil |
| XRD | X-ray diffraction |

## List of symbols

| | |
|---|---|
| Absorbance | $Ab$ |
| Area of crystal | $A$ |
| Area of sphere | $A_s$ |
| Average radius for $Fe_3O_4$ particles | $r_{Fe}$ |
| Average radius for $Fe_3O_4$-$SiO_2$ particles | $r_{Si}$ |
| Concentration change | $\Delta C$ |
| Concentration of titrant | $C$ |
| Crystal density | $\rho q$ |
| Density of ironoxide | $\rho_{Fe}$ |
| Density of silica | $\rho_{Si}$ |
| Density of sphere | $\rho_s$ |
| Equilibrium concentration | $C_e$ |
| Frequency change | $\Delta f$ |
| Initial concentration | $C_0$ |
| integer | $n$ |
| Intensity after going through sample | $I$ |
| Intensity before going through sample | $I_0$ |
| Lattice spacing | $d$ |
| Mass change | $\Delta m$ |
| Mass of crude oil | $m_{oil}$ |
| Mass of benzoic acid | $m_{BA}$ |
| Mass of sphere | $m_s$ |
| Mass propylamine | $m_{PA}$ |
| Measured specific area | $S_T$ |
| Molar absorptivity | $\varepsilon$ |
| Molecular weight 4-heptylbenzoic acid | $M_{PA}$ |
| Molecular weight benzoic acid | $M_{BA}$ |
| Molecular weight pottasium hydroxide | $M_{KOH}$ |
| Molecular weight propylamine | $M_{HBA}$ |
| Number of alkoxy groups in the silane not grafted onto the silica surface | $k$ |
| Number of carbons in ODS grafted onto surface | $C_{InODS}$ |
| Path length through sample | $l$ |

| | |
|---|---|
| Radius of sphere | $r_s$ |
| Resonance frequency | $f0$ |
| Scattering angle | $\theta$ |
| Shear velocity of the crystal | $\upsilon q$ |
| Specific mole | $n_{ODS}$ |
| Specific mole aminopropyltrimethoxysilane | $n_{APTMS}$ |
| Specific mole carbon | $n_C$ |
| Specific mole carbon from aminopropyltrimethoxysilane molecule | $n_{C\text{-}APTMS}$ |
| Specific mole hydrogen | $n_H$ |
| Specific mole nitrogen | $n_N$ |
| Specific mole of reacted hydroxylgroups | $n_{\text{-}OHr}$ |
| Specific mole of unreacted hydroxylgroups | $n_{\text{-}OHur}$ |
| Specific surface area | $S$ |
| Surface concentration | $\Gamma$ |
| Surface concentration of particles at sample point i | $\Gamma_i$ |
| Theoretical specific surface area | $S_M$ |
| Theoretical specific surface area for $Fe_3O_4$ particles | $S_{FeT}$ |
| Theoretical specific surface area for $Fe_3O_4$-$SiO_2$ particles | $S_{SiT}$ |
| Total area of particles of concentration point i | $A_{Ti}$ |
| Volume of sample | $V$ |
| Volume of sphere | $V_s$ |
| Volume of titrant at infliction point | $V_{eq}$ |
| Wavelength | $\lambda$ |

# Contents

Preface ..... 1
Abstract ..... 3
Sammendrag ..... 5
List of abbreviations ..... 7
List of symbols ..... 9
Project background ..... 15
1. Introduction ..... 17
1.1. Naphthenic acids and formation of metal naphthenates ..... 18
1.2. Flow assurance challenges related to the presence of naphthenic acids ..... 18
1.2.1. Prevention of naphthenate deposit formation ..... 19
2. Functionalization of magnetic nanoparticles ..... 21
2.1. Magnetic nanoparticles ..... 21
2.2. Silica coating ..... 23
2.3. Amino-functionalization ..... 24
3. Advanced characterization of magnetic nanoparticles ..... 27
3.1. Gas adsorption ..... 27
3.2. Electron microscopy ..... 27
3.3. X-ray diffraction ..... 28
4. Applications of magnetic particles in petroleum industry ..... 29
4.1. Oil spills (from water phase) ..... 29
4.2. Emulsion separation (from both oil and water phase) ..... 32
4.3. Removal of unwanted compounds (from both oil and water phase) ..... 35
4.4. Other applications ..... 36
4.4.1. Enhancing reservoir imaging ..... 36

4.4.2. Asphaltene flocculating agents ..... 36
4.4.3. Increasing flow assurance ..... 37
4.4.4. Release of trapped oil ..... 37
5. Materials and Methods ..... 38
5.1. Materials ..... 38
5.2. Methods ..... 38
5.2.1. Synthesis of $Fe_3O_4$ nanoparticles by co-precipitation ..... 38
5.2.2. Coating of the $Fe_3O_4$ nanoparticles with silica ..... 39
5.2.3. Amino functionalization of $Fe_3O_4/SiO_2$ nanoparticles ..... 39
5.2.4. Adsorption experiments ..... 41
5.2.5. Particle recycling ..... 41
5.3. Selectivity of amino-functionalized particles ..... 42
5.4. Nanoparticle and crude oil characterization ..... 42
5.4.1. Gas adsorption ..... 42
5.4.2. Total acid number ..... 43
5.4.3. Electron microscopy ..... 43
5.4.4. Elemental analysis ..... 44
5.4.5. Fourier transform infrared spectroscopy ..... 44
5.4.6. Asphaltene precipitation ..... 44
5.4.7. Ultraviolet-visible spectroscopy ..... 45
5.4.8. Quartz crystal microbalance ..... 45
6. Results and discussion ..... 47
6.1. Selectivity of amino-functionalized particles ..... 47
6.1.1. Total acid number ..... 47
6.1.2. Elemental Analysis ..... 48
6.1.3. Fourier transform infrared spectroscopy ..... 49
6.1.4. Asphaltene precipitation ..... 49

6.1.5. Ultraviolet-visible spectroscopy ..... 50
6.2. Synthesis and characterization of magnetic nanoparticles ..... 53
6.2.1. Synthesis of $Fe_3O_4$ particles by co-precipitation ..... 54
6.2.2. Silica coating of $Fe_3O_4$ particles ..... 55
6.2.3. Surface functionalization of $Fe_3O_4/SiO_2$ particles ..... 55
6.2.4. Gas adsorption ..... 56
6.2.5. Fourier transform infrared spectroscopy ..... 58
6.2.6. Elemental analysis ..... 59
6.2.7. Transmission electron microscopy ..... 65
6.3 Adsorption capacity of functionalized nanoparticles ..... 72
6.3.1. Quartz crystal microbalance ..... 74
6.4. Particle recycling ..... 79
7. Conclusions ..... 80
8. References ..... 82
9. Appendices ..... I
9.1. Instruments ..... I
9.2. Figures ..... II
9.3. Tables ..... V

## Project background

The main goal of the Vista project is to establish new methods for both preventing formation and facilitating removal of the metal naphthenates present in crude oil, at oil/water interface and in the aqueous phase. Rapid innovations in the nanoparticle research have generated the interest to the newly designed materials with properties beneficial to various industries. Among the wide range of nanoscale materials, magnetic nanoparticles may become very useful for the petroleum industry. In this project, attempts are being made to develop new methods for extracting naphtenic acids (NA) and metal naphthenates from the crude oil by using magnetic nanoparticles. Surface functionalization of those materials can widen the variety of possible applications. One of the main advantages of this technology is that the magnetic nanoparticles can be recovered at the end of the process by an external magnetic field and then be reused.

The newly developed methods will be based on the application of the magnetic nanoparticles for extraction of NA before formation of the metal naphthenates (mitigation strategy) as well as removal of the metal naphthenates (remediation strategy). The nanoparticles are designed according to their affinity to the carrying phase (oil, water, or interface). The new methodology will bring concepts with the following advantages:

- The FMN will be recovered at the end of extraction, regenerated and recycled.
- No toxic chemicals will be lost into oil or produced water as the FMN will be recovered at the end of the process.

A previous Master's student, Mia Ronander [1] has in 2015 performed part of the work contributing to the Vista project. Commercial nanoparticles were purchased and tested with respect to particle size and surface area, and were found not to fulfil the requirements for studying adsorption of NA. The size of the particles was estimated to be 3.3 μm, and the specific surface area was calculated to be 1.4 $m^2/g$ revealing that the commercial product was not fit for studying adsorption due to too small surface area of the particles.

Therefore, synthesis of new particles was required. $Fe_3O_4$ magnetic nanoparticles were successfully synthesized by co-precipitation, and coated with a silica layer via a sol-gel approach. The synthesized nanoparticles had magnetic properties, and were attracted when a magnetic field was applied. The obtained particles had a yield of 109 %. The coating with a silica layer had a satisfying yield from 90 % to 102 % for all batches, which was reflected in the good separation ability from the liquid. The crystallinity of the $Fe_3O_4$ nanoparticles was estimated by X-ray diffraction (XRD), and had a good comparability with the standard $Fe_3O_4$ values. The XRD peaks were also used to calculate the average particle size, and the average

size was estimated to be 12 nm. The diameter was used to estimate the specific surface area of the synthesized material, and was found to be 98 $m^2/g$. Characterized by gas adsorption analysis enabled the measurement of the specific surface area. The $Fe_3O_4$ MNP and $Fe_3O_4/SiO_2$ nanoparticles had a large specific surface area of approximately 100 $m^2/g$, especially compared to the low values of the commercial particles. The measured specific surface was very close to the estimated value from the XRD measurements. The silica covered nanoparticles were used for studying NA adsorption in octane. The model NA were adsorbed from octane, and two absorption curves with similar trends were obtained. The adsorption curves increased in the start and then levelled out from concentration at approximately 0.2 g/L to 0.9 g/L NA in octane revealing successful adsorption of the model NA.

From that it was concluded that the designed nanoparticles were suitable for carrying out the proposed experiments and for future surface modifications. Functionalization of the silica covered nanoparticles was suggested as the next step in studying adsorption of NA from the model oil and real crude oil systems.

A literature study in the current thesis is aiming to review the role of NA in production problems associated with formation of metal naphthenates and possible ways for extraction of the NA by use of magnetic nanoparticles. Different amino-functionalization reactions are evaluated for modification of the silica surfaces. Various types of magnetic nanoparticles are reviewed for other possible applications in the crude oil production and processing.

Based on the findings from the literature review, an amino-functionalization of the silica-coated particles was found to be one of the most promising methods to improve adsorption capacity and selectivity of NA for the particles. First step was to evaluate selectivity of amino groups towards NA in the real crude oil. The extraction was performed using commercial silica particles grafted with a known amount of amino fractions. The results confirmed that the amino groups selectively attracted acidic fractions to a much higher degree than other components in the oil. Two different amino-functionalization reactions were carried out for modification of the synthesized magnetic nanoparticles. The obtained samples were tested with respect to various parameters, such as visual magnetic properties, specific surface area, adsorption capacity, visual appearance, size and thickness of the coating layer. A newly developed recycling procedure for the nanoparticles were performed.

# 1. Introduction

Calcium naphthenate is a troublesome deposit that can form during crude oil production and processing in the systems that are handling an acidic crude oil with a total acid number (TAN) [2] higher than 0.3. High TAN crude oils are currently being produced in several major regions, including the North Sea, the Gulf of Mexico, California, Venezuela, West Africa, and China, and becoming more and more common, especially in deep-water production. "Calcium" naphthenate is actually a generic term used to describe deposits containing calcium, sodium, magnesium, iron and other metal naphthenates, and possibly asphaltenes, scale, and other solids. Naphthenate deposits typically form when naturally occurring NA [3] in the crude oil come in contact with metal ions (such as calcium) in the produced water under the right conditions of pH and temperature. It is important to consider oil, water, and the interface between them as a whole system when dealing with problems associated with the presence of those acids. Metals (primarily $Ca^{2+}$) can be dissolved in crude oils by formation of complexes with indigenous NA. Being a source of contamination, these metal naphthenates will significantly affect the crude oil quality. The metal naphthenates are also surface/interfacially active compounds which tend to accumulate at W/O interfaces and stabilize emulsions, or form calcium naphthenate deposits (case of ARN). This will cause operational problems ranging from oil treating problems and poor water quality to heavy deposits that can plug lines and valves [4].The NA and naphthenates can also be present in the water phase causing environmental problems.

Therefore, development of the methods for effective extraction of NA from crude oils is economically and environmentally valuable. Existing processes for NA removal has varying degrees of success, and there is a need for more efficient and environmentally friendly methods to decrease the NA content and, thus, the crude oil value.

In this thesis, attempts are made to review different silica coating strategies and amino-functionalization mechanisms that can be used for extracting the NA from the model and crude oils by using magnetic nanoparticles (MNP). One of the main advantages of this technology is that the MNP can be recovered at the end of the process and reused for new extractions. Also use of MNP in other processes during crude oil production and processing is reviewed to create a full overview of the possible applications.

## 1.1. Naphthenic acids and formation of metal naphthenates

NA are complicated mixtures found in many crude oils, but becoming troublesome only in higher concentrations. Majority of those acids are C10–C50 monoacids with 0–6 fused saturated rings and the carboxylic acid group attached to a ring with a short side chain [5]. In addition, a very small part of them is composed of molecules with four acid functions, named tetra-acids or ARN, responsible for the formation of calcium naphthenate deposits in the oil fields [1, 3] Figure 1.1. The ARN species is believed to be present in crude oils in very low concentrations of less than 20 ppm and exhibit high interfacial activity. It has to be mentioned that the ARN naphthenic acid species, being considered to dominate in the naphthenate formation, has also been identified in the crude oils from the fields without known deposition problems [6].

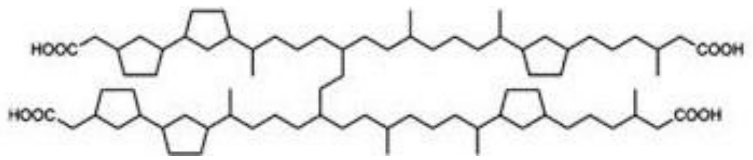


***Figure 1.1:*** *Structure of the tetrameric acid with 6 cyclopentane rings [3].*

A pressure drop typically occurs during transportation of the crude oil from reservoir to the topside process facilities. That may cause degassing of the oil and also higher pH as a result of rising levels of carbon dioxide. At high pH, a part of the NA partitions into water as calcium naphthenate and, to a lesser extent, other metal naphthenate deposits Figure 1.2. The deposits will gradually accumulate and cause problems at process facilities, especially when refining heavy crude oils with high TAN [7].

$$M^{2+} + 2RCOO^{-} \underset{k_2}{\overset{k_1}{\leftrightarrow}} [RCOO-M]^{+} + RCOO^{-} \overset{k_2}{\rightarrow} (RCOO)_2 - M$$

***Figure 1.2:*** *Schematic representation of metal naphthenate formation.*

## 1.2. Flow assurance challenges related to the presence of naphthenic acids

Flow assurance is a relatively new term, which refers to ensuring a successful and economical flow of hydrocarbons from reservoir to the point of sale and is closely linked to multiphase

flow technology. The term was introduced by Petrobras in the early 1990s in Portuguese meaning literally “Guarantee of Flow”[8].

The appearance of naphthenate deposits downhole, in pipelines, or up in the surface facilities during crude oil production and processing and also formation of stable emulsions can be named as some the most common and serious flow assurance problems[9]. Calcium naphthenate deposits from a cooler and coalescer are shown in Figure 1.3.

*Figure 1.3: Naphthenate deposits in a cooler [10] and deposits removed from a coalesce [11].*

Calcium naphthenates are neither soluble in water nor oil and have density lower than water, but higher than the oil phase. Therefore, accumulation of voluminous particles at the oil/water interface may occur and lead to costly shutdown periods and additional flow assurance challenges. It has to be mentioned that the metal naphthenates can also have some positive effect on the flow assurance effectively suppressing the growth of sulfate-reducing bacteria in sea water and protecting steel in neutral corrosive media [12].

### 1.2.1. Prevention of naphthenate deposit formation

There are several techniques currently used by industry to prevent formation of naphthenate deposits. One of the most common is addition of acid which can keep the pH low and thereby avoid naphthenate formation. The most common acids currently used for the metal naphthenate inhibition are phosphoric acid (inorganic mineral acids), acetic acid or glycolic acid (small organic acids) and dodecylbenzenesulfonic acid (DDBSA)(surfactant acids)[13].

However, addition of acids is costly, may increase corrosion problems and not environmentally friendly.

Use of special additives, such as demulsifiers or dispersants, have given encouraging results, but an additive which works well with one crude can be inefficient with another [14]. To inhibit naphthenate salt formation, special surfactants designed to inhibit the reaction with NA, can also be injected. The surfactants surround the interfacial surface between oil and water and leave no room for the NA deposit of the interface [15].

Since pressure reduction to below 10 bara will increase the water pH through loss of dissolved CO2 and promote the formation of naphthenates, water separation at high pressure prior to stabilization can be a good solution. Avoidance of plugging/deposition of calcium naphthenate deposits by careful selection of vessel internals and through consideration of bypasses around vulnerable equipment e.g. heaters, coalescers, can be a solution in certain cases.

Another approach is the catalytic decarboxylation of NA. Zhang et al.[2] showed that magnesium oxide (MgO) can enhance catalytic decarboxylation and remove some NA at low-temperatures with possibility of the process to be upgraded to a large-scale.

## 2. Functionalization of magnetic nanoparticles

Establishing new methods for both preventing formation and facilitating removal of the metal naphthenates and NA present in crude oil, at oil/water interface and in the aqueous phase are highly important for the future of the heavy oil production. Rapid innovations in the nanoparticle research have generated the interest to the newly designed materials with properties beneficial to various industries. Among the wide range of nanoscale materials, magnetic nanoparticles may become very useful for the petroleum industry.

In this work, attempts will be made to describe the best possible methods for extracting NA and metal naphthenates from the crude oil by using MNP. Surface functionalization of those materials can widen the variety of possible applications. One of the main advantages of this technology is that the MNP can be recovered at the end of the process and reused for new extractions.

### 2.1. Magnetic nanoparticles

A nanoparticle is a particle between 1 and 100 nm in size. A nanoparticle is called magnetic if it is made of a material exhibiting magnetic properties, when exposed to magnetic field. The performance of MNP largely depends on the type of material and size. A number of materials can be used for the synthesis, including iron oxides $Fe_3O_4$, pure metals Fe and Co, spinel type ferromagnets $MgFe_2O_4$, $MnFe_2O_4$, or Co $Fe_2O_4$ [16]. Chemical stabilization of these particles is usually required as they are easily oxidized in air, resulting in loss if magnetic properties and reduction of dispersibility. In many cases the stabilization strategies, such as surface coatings with polymers, surfactants, or inorganic compounds, not only protects the particles, but can also be used for further modification or functionalization [16]. Functionalization is the addition of functional groups onto the surface of a material by chemical synthesis methods. Schematic illustrations of a nanoparticle and functionalized nanoparticle are presented in Figure 2.1.

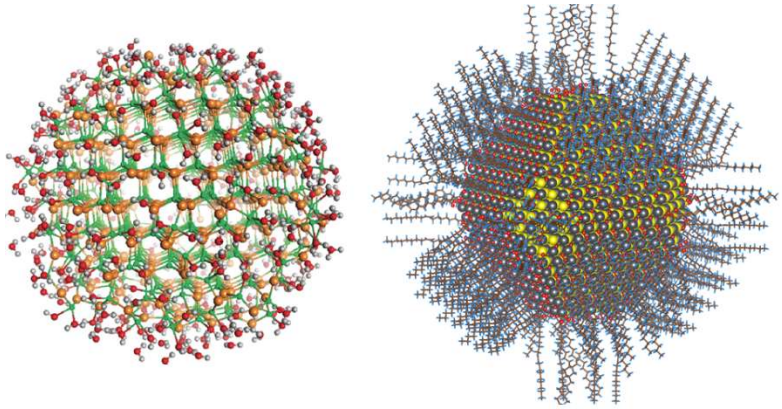

***Figure 2.1:*** *Atomic structures of a nanoparticle and functionalized nanoparticle with functional groups residing on the surface.*

Magnetic nanoparticle can be synthesized by several different methods including co-precipitation, thermal decomposition and/or reduction, micelle synthesis, hydrothermal synthesis, and laser pyrolysis techniques [16]. All of those methods can be used in the synthesis of high-quality stable magnetic nanoparticles, but some are more common than others are. Method chosen for the synthesis will depend on factor like, material, desired size of the nanoparticle, shape, porosity etc.

Bulk materials cannot be used in most fluid products unless made very small. The decrease in size affords an enormous change in surface area – a key economical aspect of nanoparticle synthesis and provides a huge interface between the constituents. The key examples of the nanoparticle properties are shown in Figure 2.2.

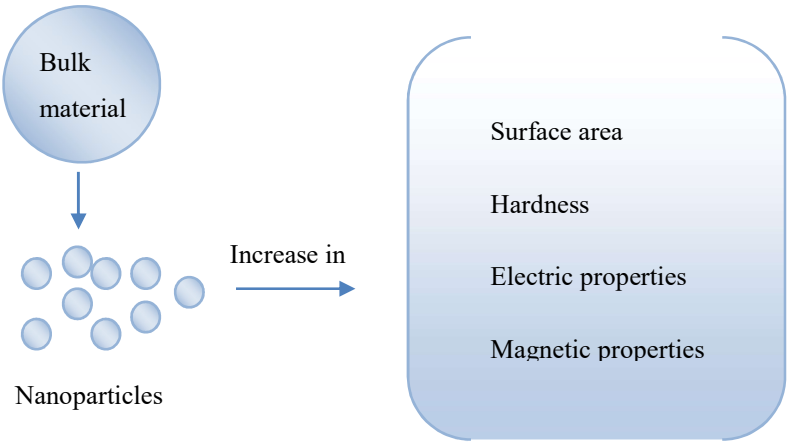


***Figure 2.2:*** *Key examples of nanoparticle properties.*

The possibility of easy separation and controlled placement of these functionalized magnetic nanoparticles by means of an external magnetic field enables their promising applications in many industrial fields. A drop in saturation magnetization and variation of

particle size may occur after surface functionalization of the MNP. These are the primary factors that affect the separation time and velocity of the MNP and have to be thoroughly studied in order to develop optimal separation procedures.

## 2.2. Silica coating

After a magnetic nanoparticle has been synthesized it needs to be protected from being oxidized in the surrounding atmosphere and chemically stabilized. Both are closely related and nanoparticle stability can be considered as a critical requirement for almost any application. Nanoparticle surface can be coated with surfactants, polymers, precious metals and also surface passivated [17, 18].

Nanoparticles with modified surfaces will exhibit novel physical and chemical properties that can be essential for future applications. Control over nanoparticle structure and interface interactions is important in this case. If iron oxide is assumed as the core, the structure of inorganically functionalized nanoparticles can roughly be divided into five types: core-shell, mosaic, shell-core, shell-core-shell, and dumbbell. Examples of the different structures are shown in Figure 2.3.

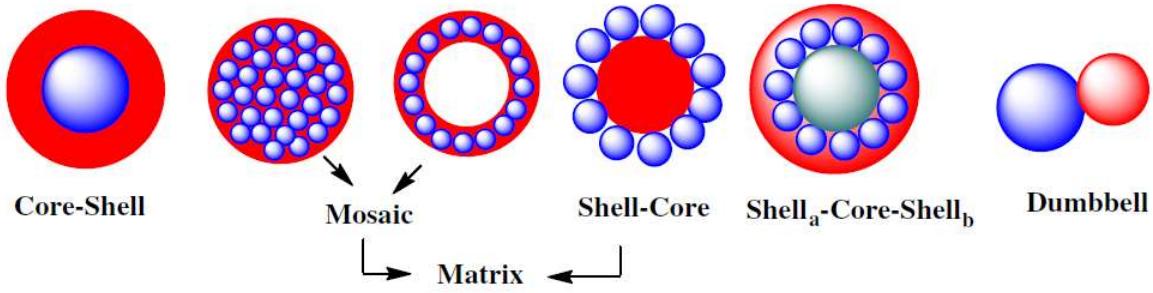


***Figure 2.3:*** *Different types of inorganically functionalized nanoparticles [19].*

In this work, we will focus on surface coating with silica as it is the most beneficial method for further amino-functionalization. Compared to other materials, silica offers several advantages, such as:

- Providing stability of iron oxide nanoparticles
- Avoiding interparticle interactions and preventing agglomeration
- Hydrophilicity of the surfaces
- Relative easiness to control shell thickness in preparation of size-tunable particles
- Binding compatibility with various biological and other ligands

There are several commonly used techniques to apply the silica coating to the surface of nanoparticles, including Stöber method, sol–gel processes, and aerosol pyrolysis [19]. In general, silica coating will contribute to the increase in size of the nanoparticles. Therefore, magnetic properties will also change. The thickness of the silica layer from 5 to 200 nm can be tuned by varying concentration of ammonia and also by modifying ratio of tetraethoxysilane (TEOS) to water. When working with nanoparticles made of pure metals, a primer is required to promote the deposition and adhesion of silica. However, in case of metal oxides the silica coating can be easily performed on the iron oxide surfaces through hydroxyl groups in the aqueous environment, especially by using the Stöber method [20] or sol–gel process [21].

The synthesis of uniform silica shell and tailored thickness in a controlled environment can be tricky. On of alternative methods to do it is by use of microemulsion, also known as water-in-oil (W/O) microemulsion process, employing three primary components: water, oil, and surfactant [22]. It has also have shown that commercially available ferrofluids can be directly coated with silica shells by the hydrolysis of TEOS [23].

## 2.3. Amino-functionalization

The functionalization of silica particles is a method for activating the surface properties of particles to fit the target applications. The amino-functionalized silica nanoparticles have wide commercial applications, including removal of pollutants/adsorption [24-26], catalysis, separation, chromatography [27], etc. The methodology of silica surface functionalization is conveniently applicable to all silica surfaces, independent of the porosity of the starting material.

The following reaction mechanism is one example of amino-functionalization that can be used for extraction of NA from the crude oils (Figure 2.4). The silica coated MNP have an advantageous ability to be functionalized by mixed ligands, with different functional groups. This property enables the surface of the nanoparticles to attract targets with different functional groups. The silica coating is functionalized with both $C_{18}$ and $NH_2$ Groups. The nanoparticles composed of $Fe_3O_4$ are coated with silica by the addition of TEOS after synthesis of the magnet core.

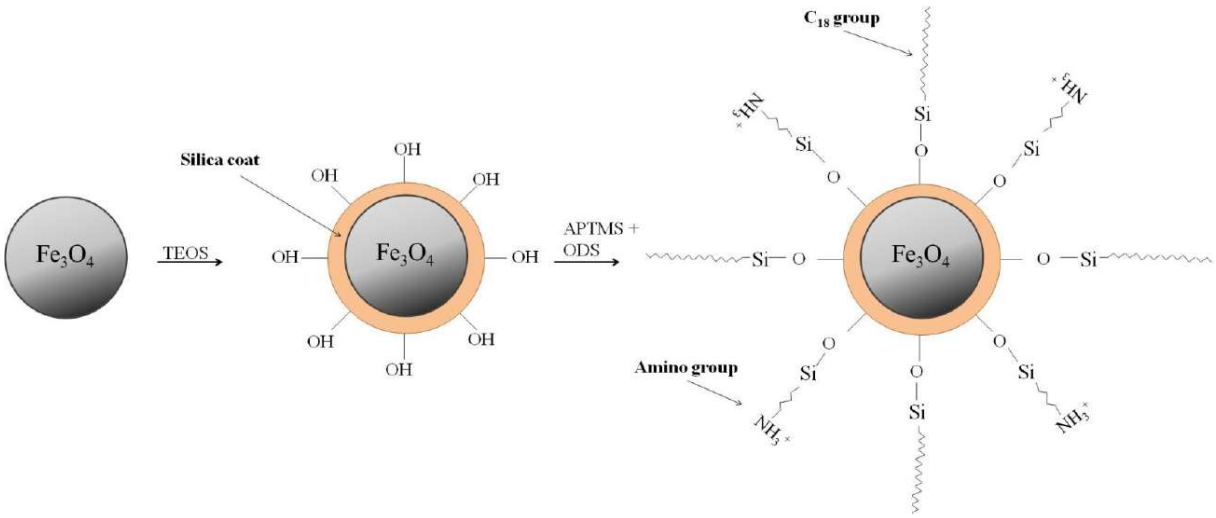


***Figure 2.4:*** *The functionalization of MNP ($Fe_3O_4$) with silica modified by C18 and amino groups[24].*

Afterwards, the silica is functionalized by octadecyltriethoxysilane (ODS) and aminopropyltrimethoxysilane (APTMS), so that the functional groups $C_{18}$ and $NH_2$ could be attached to the surface. The reaction scheme is illustrated in Figure 2.4. The current functionalization method was successful in the removal of anionic organic pollutants in acidic conditions and indicated high extraction performance. The functional groups were said to provide hydrophobic interaction and electrostatic attraction [24].

Another interesting material for extraction of NA could be mesoporous silica, a class of synthetic materials with high surface area composed of amorphous silica that is periodic on the mesoscopic length scale. The particles made of the mesoporous silica have molecular sieves with large pore diameters ranging from 2 to 50 nm and attracted a great deal of attention because of their high specific surface areas. The introduction of the amino groups onto the mesopores was carried out based on the self-assembly of anionic surfactants and inorganic precursors in the presence of aminosilane or quaternized aminosilane as a co-structure-directing agent. Those particles showed good adsorption capacity of various metal ions and exhibited potential to be used for many interesting applications [25].

The recovery and possibility of reuse of the functionalized nanoparticles is also of high importance. Amino-functionalized silica magnetite nanoparticles have been prepared and modified with 3-aminpropyltriethoxysilane (APTES). The modification was carried out by the organic solvent method in dry hexane to graft amine groups on the surface. The adsorption behavior of this novel magnetic sorbent was studied for the simultaneous removal of two

organic pollutants containing the sulfonate group in aqueous solution (from wastewaters). The FMN were regenerated by washing with 0.1 M NaOH solution without loss of properties [26].

A controlled amino-finctionalization of silica coated nanoparticles was done by Kralj et al. [28]. APTMS was grafted onto the nanoparticle surfaces in their aqueous suspensions. The surface concentration of the amino groups could be varied by increasing the amount of APTMS in the grafting process up to approximately 2.3 $–NH_2$ groups per $nm^2$.

An organic group, which is often used for amino-functionalization is 3-aminopropyl. Certain applications require adjustment of the amount of active 3-aminopropyl species on the surface of the silica. This can be done by controllable introduction of additional functional groups, such as methyl or carboxyl [28, 29]. The functionalization with the 3-aminopropyl group or with mixtures of the 3-aminopropyl and methyl groups lead to higher molar coverages of the silica surface than functionalization with the methyl group alone. The reason for these effects is that the amino group base catalyzes the hydrolysis of the alkoxysilanes and thereby enhances the reaction of the silanes with the silica surface [29].

# 3. Advanced characterization of magnetic nanoparticles

The detailed characterization of magnetic nanoparticles plays important role in the development of the nanomaterials. Nanoparticle samples have traditionally been analyzed as bulk, and compositions reported as mean values – most recent instrumentation permits chemical analysis at the single particle level. Several widely used material science techniques are applicable for the characterization. They include scanning electron microscopy (SEM), environmental SEMs, transmission electron microscopy (TEM), atomic force microscopy, X-ray diffraction (XRD), X-ray photoelectron spectroscopy (XPS), energy-dispersive X-ray analysis (EDAX), solid-state nuclear magnetic resonance spectroscopy (NMR) and many others. Some of the methods of characterization are presented in the current review.

## 3.1. Gas adsorption

The Brunauer-Emmet-Teller (BET) method was used to determine the specific surface area of the synthesized particles. The method is based on the adsorption of gas on the surface of the particles, and measuring the amount adsorbed gas at known pressure. By analyzing a known amount of particles, the specific surface area can be found. It has a particular importance for adsorption, heterogeneous catalysis, and reactions on surfaces.

## 3.2. Electron microscopy

Scanning electron (SEM) and high-resolution transmission electron microscopy (TEM) can be used for imaging magnetic nanoparticles of various sizes and compositions. While SEM has somewhat lower resolution and mostly used for imaging of the surfaces, the TEM may provide better view of the particle core. Figure 3.1 shows the TEM images of silica-coated iron oxide nanoparticles. The images clearly indicate the single-crystalline nature of the iron oxide core and the amorphous nature of the silica shell.

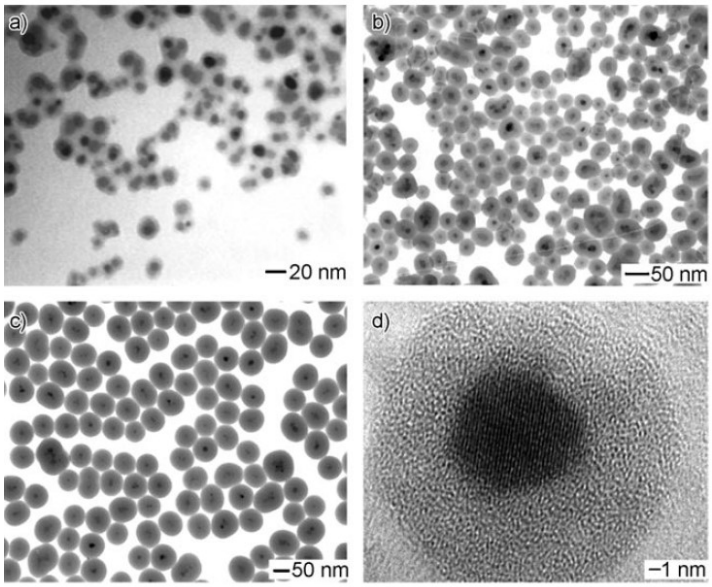


***Figure 3.1:*** *TEM images of iron oxide nanoparticles coated with silica shells of various thickness.*

The SEM requires less complicated sample preparation than TEM and can be used for imaging of the surfaces or particles agglomeration. However, due to magnetization, the nanoparticles might have to be places on a sticky carbon/copper tape before carrying out the analysis.

## 3.3. X-ray diffraction

Structural characterization can be carried out using x-ray diffraction (XRD). The analysis investigates atomic arrangement, orientation, imperfections, and provides information on structures and phases. The XRD can be used for the evaluation of the crystalline structure of the dispersed nanoparticles, a property that determines accessibility to reactive groups. This technique can contribute to identify the physical and chemical form of the nanoparticles such as different forms of iron oxides [30].

# 4. Applications of magnetic particles in petroleum industry

Magnetic nanoparticles exhibit many interesting properties that can be exploited in a variety of applications during crude oil production and processing. This review focuses on the recent developments in preparation, structure, and magnetic properties of naked and surface functionalized iron oxide nanoparticles related to their possible applications during industrial processing of petroleum.

Many of the applications of magnetic particles in the petroleum industry follow a similar pattern. First, the particle is introduced to a medium. Then it does what it is specialized to do, be it to adsorb a specific chemical with its surface or a functional group grafted at the surface, go to a specific interface or something else. Secondly a magnetic field is introduced and the magnetic particles aggregates as close to the magnet as possible. Then the particle is separated from the other medium. There are exemptions to this pattern, like magnetic heating of pipes.

## 4.1. Oil spills (from water phase)

Petroleum spills pose a problem to the environment and can be detrimental to the local fauna. Over 20000 oil spills are reported to the US government each year [32]. After an oil spill into water, the immediate methods to the bulk recovery clean-up involve processes such as booms, skimmers, and removal through suction. The leftover contamination is usually a low oil concentration in the water which appears as a thin film on the surface of the water (0.04-50 μm) [33]. To remove the low concentration parts, sorbents and bioremediation are often used; these methods are impractical because of cost and time [34]. An alternative method may be to use the magnetic nanoparticles to separate the oil from the water.

Pavia-Sanders et al. [35] constructed well-defined magnetic shell cross-linked knedel-like nanoparticles (MSCK) with hydrodynamic diameter of around 70 nm. These nanoparticles were designed to separate oil from water. The overview of this process can be seen in Figure 4.1.

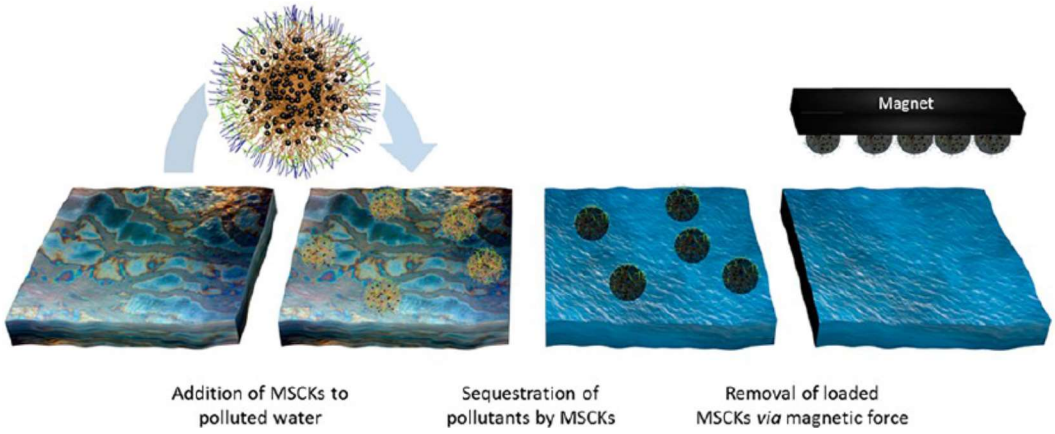


***Figure 4.1:*** *Separation of oil contamination from water using MSCK [35].*

The MSCK synthesis involved the co-assembly of amphiphilic block copolymers and oleic acid-stabilized magnetic iron oxide nanoparticles. A schematic illustration of this is shown in Figure 4.2.

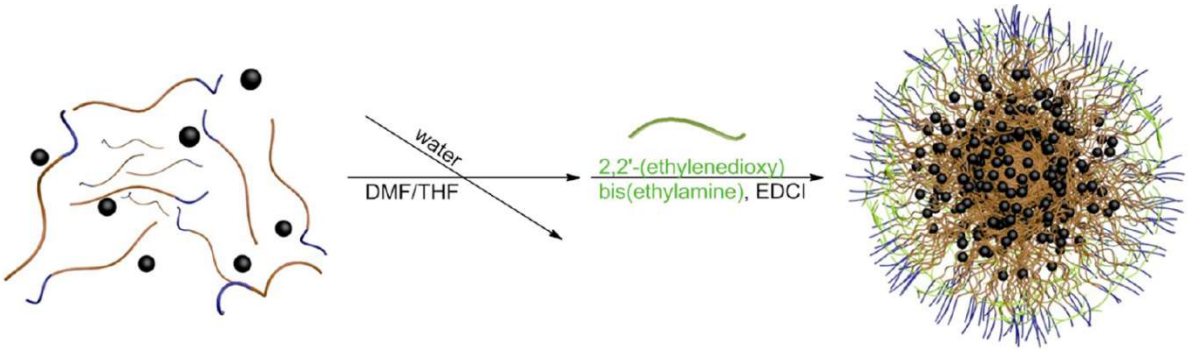


***Figure 4.2:*** *Schematic view of the construction of MSCK [35].*

Pavia-Sanders and colleagues found that the oil sorption capacity of the MSCK were 10-fold its dry weight (1 mg MSCK adsorbed 10 mg oil containment). The reusability was also tested and the nanoparticles were found highly effective, even though they had gone through chemical changes during its recycling process. Compared to methods currently in use for removal of oil containments, MSCK is about twice as efficient when it comes to the loading capacity.

Atta et al. [36] have also investigated the application of MNP for crude oil spills in water. They synthesized $Fe_3O_4$ nanoparticles coated with rosin amidoxime. These particles were tested as a crude oil collector in an aqueous environment and separated with a magnetic field. It was concluded that they may serve as a substitute for the current technologies used today.

Another study investigating the MNP as oil spill sorbents was done by Yu et al. [37]. The $Fe_3O_4$ magnetic core was coated with porous silica (MPSS). The silica coatings were made with hexadecyl trimethylammonium bromide (CTAB) as a template and TEOS as the silica source. To make the silica coating porous vinyltriethoxysilane (VTES) was used. An overview of the synthesis process is given in Figure 4.3.

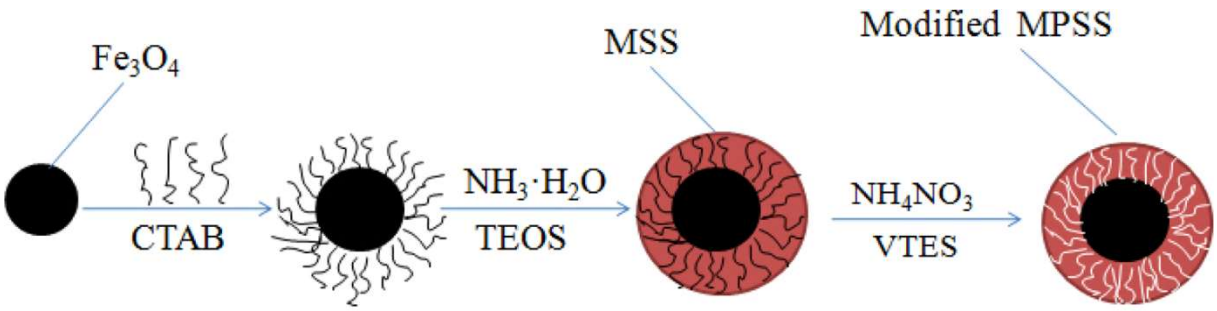


***Figure 4.3:*** *Overview of the synthesis of MPSS [37].*

The concept of the oil sorption cycle is quite similar to the procedures mentioned above, and it is shown in Figure 4.4. First the modified MPSS are placed in the contaminated system. They adsorb the oil residues, mixed with alcohol and attracted to a magnet. The particles are cleaned and drying and can be reused for later adsorptions.

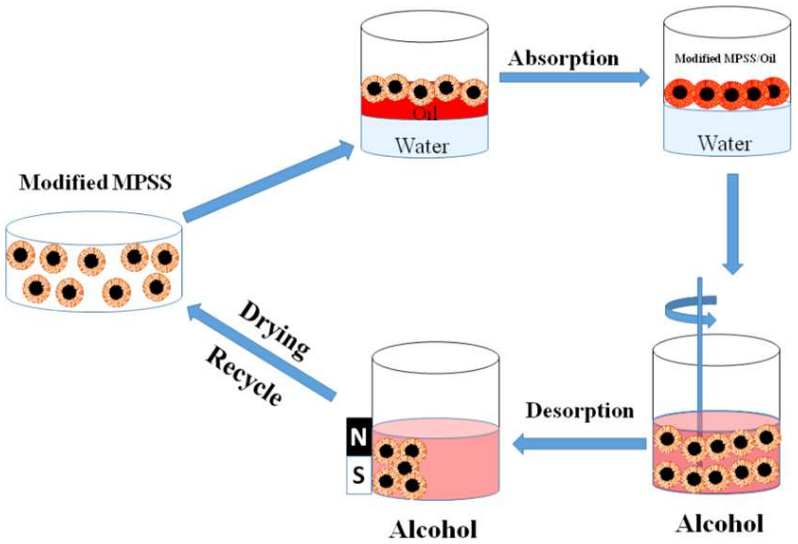


***Figure 4.4:*** *Overview of the recycling process of the MPSS [37].*

Yu et al. [37] found that the MPSS showed a fast magnetic response, superoleophobicity, and temperature stability for removal of all kinds of oils from a water surface. They reported an absorption capacity of up to 11.51 times its own dry weight. The MPSS kept its hydrophobicity after 20 recycling cycles. As mentioned in the previous magnetic oil spill studies, this one also claims that the magnetic nanoparticles are a promising candidate for oil spill adsorbents.

## 4.2. Emulsion separation (from both oil and water phase)

Majority of the produced crude oils are initially in the form of an emulsion, water-in-oil (W/O) or oil-in-water (O/W) [38]. These emulsions might be very stable because of interfacially active materials, such as asphaltenes, resins, NA and solid particles [39], which are naturally present in the crude oil. It can also be intentionally added surfactants to increase oil recovery. These emulsions may pose several problems both in upstream and downstream processes.

Some examples are flow assurance problems or catalyst poisoning in the refinery. Chemical demulsifiers seek to be more surface active than the already interfacial active compound that is in the emulsion. When the demulsifier is at the interface it may change the interfacial properties, such as interfacial tension, mechanical strength, elasticity, and thickness of the interfacial films. This may lead to flocculation and or enhanced coalescence [40, 41]. For a magnetic demulsifier the added effect is when there is a droplet surrounded by interfacially active MNP and there is an externally magnetic field applied, it will help to separate the emulsion in a shorter time interval.

Peng et al. [42] have studied a novel magnetic demulsifier for water in diluted bitumen emulsion. Peng and co-workers prepared ethyl-cellulose-grafted $Fe_3O_4$ nanoparticles (M-EC). The M-EC consisted of interfacially active ethyl cellulose on the surface of a chemically modified $Fe_3O_4$ nanoparticle. These particles were tested to help separate water from a W/O emulsion. Figure 4.5 shows a schematic illustration of the separation process. First the M-EC are added to the emulsion, and the surface active M-EC surrounds the water droplet. The water drop surrounded by M-EC is then separated from the bitumen emulsion using an applied magnetic field. The M-EC is then recycled by washing with chloroform.

Peng et al. [42] showed that with an addition of 1.5 wt % M-EC and magnetic separation from an emulsion of 2.5-25 wt % water in naphta-diluted bitumen. A removal of more than 93% of the water was achieved. The settling time was significantly shorter when a magnetic field was applied. After recycling 10 times the M-EC showed no significant drop in efficiency

and the particles were shown to be chemically stable. The group also tried to apply M-EC to industrial bitumen froth. More than 80% of the water in the original bitumen was removed after 2 min of an applied magnetic field. They concluded that it might be the new direction for removing emulsified water from diluted bitumen.

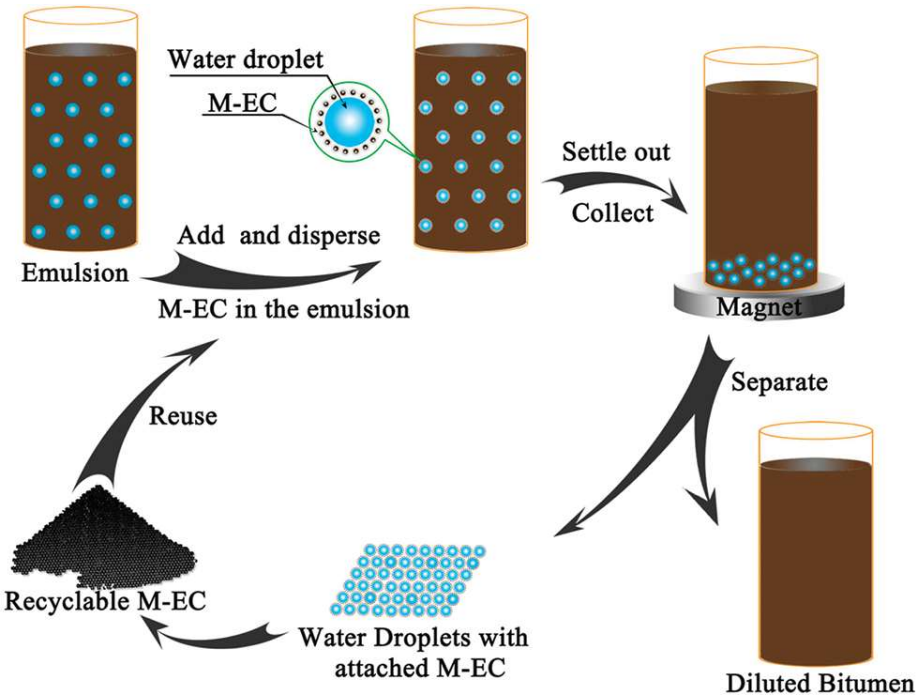


***Figure 4.5:*** *Schematic illustration of the demulsification process using M-EC [42].*

Ali et al. [43] have also studied the possibility of using a magnetic inerfacially active component to dewater crude oils. They synthesized a composite nanoparticle with a raspberry like structure, consisting of a $Fe_3O_4$ core and an interfacially active block co-polymer shown in Figure 4.6.

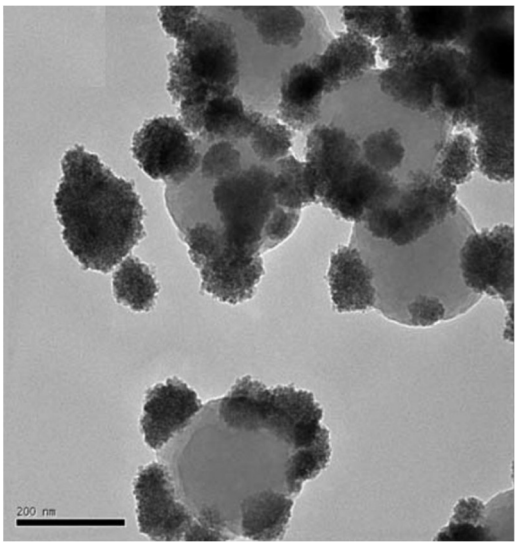


***Figure 4.6:*** *Rasperry like composite nanoparticle [43].*

The process of the dewatering performed by Ali et al. is similar to that of Peng and co-workers, and is shown in Figure 4.7. The magnetic composite material is introduced into the water oil mixture and is left over a given time with an applied magnetic field at the bottom of the sample. After the separation, the magnetic particles were recycled by solvent washing.

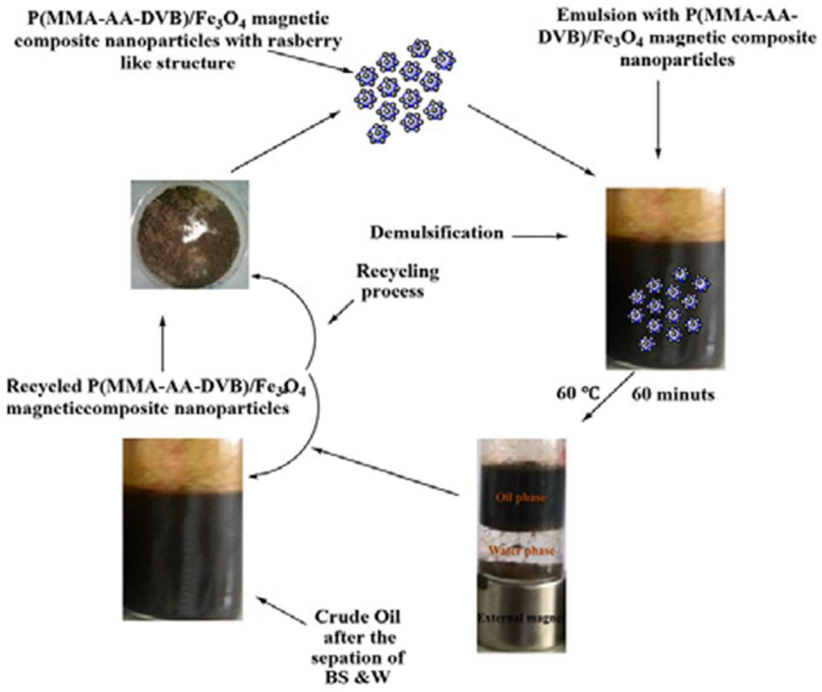


***Figure 4.7:*** *Dewatering process with raspberry like magnetic nanoparticles [43].*

Ali et al. found that the strong magnetic response of the magnetic nanoparticle at the oil water interface enhanced the coalescence of the emulsified water in the crude oil. They also

concluded that the separation efficiency of the nanoparticles after recycling 5 times was about the same as initial.

Liang et al. [44] have explored the demulsification of diluted crude O/W nanoemulsions. Single-layer oleic acid-coated magnetite particles were used as a demulsifier for cyclohexhane-diluted crude O/W emulsion. An external magnetic field was applied to attract the partciles. The group of Liang studied the dependency of concentration, wettability of the demulsifier and the pH as a function of the demulsification efficiency. An overview of the process is given in Figure 4.8.

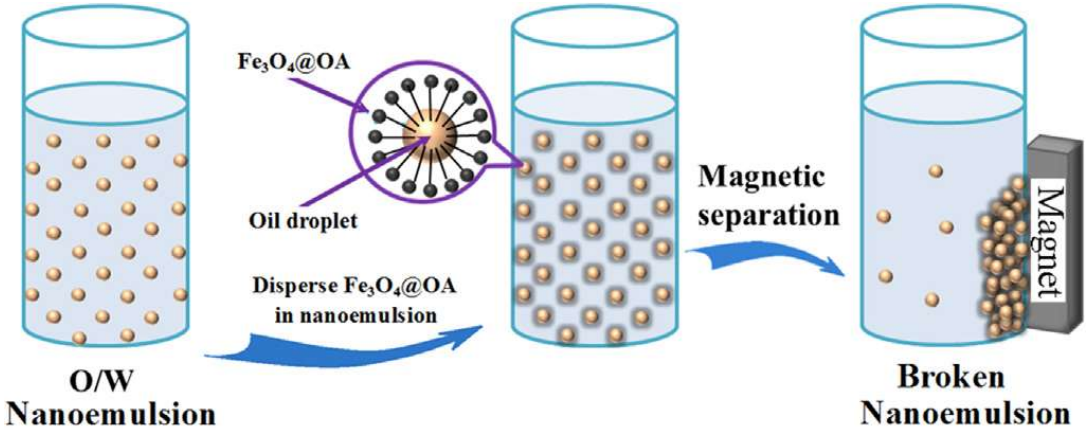


***Figure 4.8:*** *Overview of the demulsification of an oil-in-water demulsification using oleic acid coated nanoparticles [44].*

Liang and his group found that with increasing concentration of nanoparticles the demulsification efficiency increased and reached as high as 97%. A maximum demulsification efficiency was obtained with a water contact angle of about 90 degrees. For the pH range of 4.0-7.5 there was no significant change in the demulsification efficiency, but in the pH interval of 8.0-11.0 it gradually decreased.

## 4.3. Removal of unwanted compounds (from both oil and water phase)

Large amounts of water are produced in the recovery of oil and it seems that it will only increase with time. This produced water may contain significant amounts of highly dispersed oil droplets and also cations, such as $Ca^+$, $Mg^+$ and $Na^+$. The produced water needs to be treated before it can be safely disposed. A modification can also be applied before it is reinjected in the crude oil reservoir, because of the presence of cations which may significantly reduce the oil recovery [45].

Prigiobbe et al. [45] presented a study of an efficient method for removing "contaminants" from produced water by using FMN. Both highly stable oil droplets and cations may be removed with this method. Prigiobbe looked at a MNP polyacrylic acid grafted to its surface for removal of the $Ca^{+}$ cation from the produced water. The separation process is as follows: the FMN are dispersed into the produced water, $Ca^{+}$ adsorb to the acidic sites of the FMN, a magnetic field is introduced and FMN with the adsorbed cations attached to them feels the force from the magnetic field and groups together. The water and FMN are separated and the FMN are regenerated by re-suspending them in an acidic solution to remove the $Ca^{+}$ cations. Prigiobbe concluded that this method is promising compared to the conventional methods.

A method to remove oil droplets from produced water has been studied by Ko et al. [46]. They tested the ability of magnetically removing the oil with a cationic surface coated MNP. Ko and co-workers performed batch-scale experiments with 5 wt % decane in water emulsions, which have negative surface charges. The reported efficiency was about 85 to 99 % of the initial efficiency depending on the different experiment conditions. An experiment was also performed with an anionic surface coated MNP. It was not successful, which indicates that the electrostatic attraction between emulsion and MNP control the attachment of MNP to the droplet surface.

## 4.4. Other applications

### 4.4.1. Enhancing reservoir imaging

Surface coated superparamagnetic nanoparticles are capable of flowing through a micron-size pored reservoir over a long distance with little retention [47]. These particles change the magnetic permeability of the flooded region, and therefore can be used to enhance imaging of hydrocarbon reservoirs. Rahmani et al. [47] studied a simulation of the flow of a "ferrofluid" slug (a colloidal suspension of superparamagnetic nanoparticles) through a heterogeneous reservoir. They did this to evaluate the possibility of enhancing the imaging of the reservoir.

### 4.4.2. Asphaltene flocculating agents

Oliveira et al. [48] have examined the possibility of using a chemically modified cobalt ferrite nanoparticle as an asphaltene flocculating agent. Heavy organic compounds in crude oil, like waxes, resins and asphaltenes can cause problems during the production, transport and storage of the product. Problems, such as crystallization and deposition, can be encountered quite often [49]. Oliveira and co-workers modified cobalt ferrite nanoparticles with acid-base reactions

using DDBSA in order to increase its lipophilicity, meaning a better interaction between the nanoparticles and the asphaltenes. This increased interaction promotes association among the asphaltenes and decreases the asphaltene precipitation onset. Oliveira and colleagues also suggested that the superparamagnetic property of the nanoparticles can be used to magnetically remove the asphaltenes deposits before the refining process.

### 4.4.3. Increasing flow assurance

A frequent problem in oil well production is wax deposits. Classical methods to conquer this problem are frequent scraping and hot oil operation with help of coiled tubing unit. Haindade et al. [50] have proposed an alternative method to fight the wax deposits in production tubing problem. The technique involves Co-Ni nanoparticles combined with a polymer to be pumped between the production tubing and the casing when the pipe is first laid. So the suspended nanoparticles stay in between the casing and the pipe for the life time of the tube. If an oscillating magnetic field is applied outside of the tube, it will cause the superparamagnetic nanoparticles to vibrate and get heated. This generated heat will cause the wax deposits to melt. Haindade concludeed that this technique shows promise but more research is needed.

Mehta et al. [51] have evaluated a similar approach to the flow assurance problem. Instead of a nanoparticle suspension, they used a paint with $Fe_3O_4$ superparamagnetic nanoparticles. Mehta and co-workers also took advantage of the heating by vibration, when an oscillating magnetic field is applied.

### 4.4.4. Release of trapped oil

In enhanced oil recovery a challenge is to get out trapped oil in a porous reservoir. Soares et al. [52] have studied the possibility of injecting superparamagnetic ferrofluids into oil reservoirs. They tried to mobilize the residual oil under an applied magnetic field by wetting ferrofluids. This was done using 2D simulations.

# 5. Materials and Methods

## 5.1. Materials

Aqueous ammonium hydroxide (28-30 %), octane (98 %), ethanol (96 and 99.8 %), iron(II)chloride (98 %), iron(III)chloride (97 %), hydrochloric acid (37 %), tetraethyl orthosilicate (98 %) (TEOS), 4-heptylbenzoic acid (HBA), aminopropyltrimethoxysilane (97 %) (APTMS), n-octadecyltriethoxysilane (ODS), anyhydrous toluene (99,8 %), propylamine (99 %) and sodium hydroxide were all reagent grade and purchased from Sigma-Aldrich, Norway. Isolute $NH_2$ particles used to test adsorption selectivity of amino groups in crude oil were purchased from Biotage, Finland (with parameters given in Table 5.1). Heidrun crude oil from the Norwegian continental shelf was the medium for selective adsorption of NA. HBA in octane was used as a model system mimicking real crude oil containing indigenous NA. All solutions were prepared with ultrapure Milli-Q water.

***Table 5.1:*** *Parameters of Isolute $NH_2$.*

| **Particle** | **$NH_2$ isolute** |
|---|---|
| Particle exchange capacity (mmol/g) | 0.51 |
| Specific surface area ($m^2$/g) | 480 |
| Pore diameter (Å) | 56 |
| Average particle diameter (μm) | 55 |

## 5.2. Methods

### 5.2.1. Synthesis of $Fe_3O_4$ nanoparticles by co-precipitation

$Fe_3O_4$ nanoparticles were synthesized by co-precipitation [24]. $FeCl_3$ (20 mL, 1 M, in 0.2 M HCl) and $FeCl_2$ (20 mL, 0.5 M in 0.2 HCl) were mixed and added dropwise within 5 minutes to a magnetically stirred solution of sodium hydroxide (1.5 M, 80 °C) contained in a three neck flask with an Allihn condenser over. The solution was in a nitrogen surrounding. The solution was stirred for 20 minutes at 80 °C and subsequently cooled to ambient temperature by removing it from an oil bath. The nanoparticles were washed in MilliQ-water and separated with the help of a magnetic field. The first batch of $Fe_3O_4$ was dried under nitrogen at 60 °C

and stored in a screw on top vial. The second batch was just stored in Milli-Q water. The third batch was stored in a solution of HCl (0.01 M).

### 5.2.2. Coating of the $Fe_3O_4$ nanoparticles with silica

The silica coating was applied to the surface of the $Fe_3O_4$ particles through a sol-gel approach described in [24]. $Fe_3O_4$ particles (0.2 g) suspended in HCl (100 mL 0.1 M) were activated in an ultra-sonication bath for 25 min. The suspensions were mixed with ethanol (160 mL), Milli-Q water (40 mL) and aqueous ammonia (2.0 mL) in an Erlenmeyer flask. TEOS (0.2 mL) was added under magnetic stirring. The sample was sealed and stirred for 6 hours at room temperature. The particles were washed with a 50/50 water/ethanol mixture several times. The obtained $Fe_3O_4/SiO_2$ particles were stored in a water/ethanol suspension. Before the functionalization experiment, they were dried under nitrogen at 60 °C.

### 5.2.3. Amino functionalization of $Fe_3O_4/SiO_2$ nanoparticles

$Fe_3O_4/SiO_2$ particles were functionalized with ODS and APTMS in a 1:1 mole ratio by two different methods:

1. $Fe_3O_4/SiO_2$ particles (0.8 g, dried) were dispersed in 80 mL of anhydrous toluene by a 30 min long ultra-sonication. ODS (0.400 mL) and APTMS (0.145 mL) were added under manual stirring and sealed in an autoclave, acid digestion vessel model 4748 from Parr Instrument company. The autoclave (Figure 5.1) was placed in a heating cabinet (120 °C) for 8 hours and then cooled at room temperature. The particles were washed with ethanol several times and stored in ethanol.

***Figure 5.1:*** *Autoclave experimental setup.*

2. An exact same experiment was performed to functionalize the nanoparticles, but instead of using anhydrous toluene in an autoclave, anhydrous xylene (120 °C) in a three neck flask with magnetic stirring and an Allihn condenser on top. The solution was in a nitrogen atmosphere (Figure 5.2). The particles were also stored in ethanol.

***Figure 5.2:*** *Experimental setup for xylene reaction.*

The two methods were later compared by means of elemental analysis, ultraviolet-visible spectroscopy (UV-vis) adsorption, quartz crystal microbalance (QCM), specific surface area and transmission electron microscopy. An overview of all the different batches with a batch ID number are given in Table 5.2. The batch ID number system is on the form A.B.C-t/x, where A indicates from which naked nanoparticle batch, B indicates from which silica coating batch, C indicates from which functionalization reaction batch, x and t indicates if the functionalization reaction was done in xylene or toluene respectively.

***Table 5.2:*** *Batch ID numbers of the different nanoparticles.*

| Type of particle | Batch ID number | Type of storage for particles |
|---|---|---|
| $Fe_3O_4$ | 1. | Dried |
| $Fe_3O_4$ | 2. | Stored in water |
| $Fe_3O_4$ | 3. | Stored in 0.01 M HCl |
| $Fe_3O_4/SiO_2$ | 1.1. | Dried |
| $Fe_3O_4/SiO_2$ | 2.2. | Stored in water/ethanol |
| $Fe_3O_4/SiO_2$ | 3.3. | Stored in water/ethanol |
| $Fe_3O_4/SiO_2$ $NH_2/C_{18}$ | 1.1.1-t. | Dried |
| $Fe_3O_4/SiO_2$ $NH_2/C_{18}$ | 3.3.2-t. | Stored in ethanol |
| $Fe_3O_4/SiO_2$ $NH_2/C_{18}$ | 3.3.1-x. | Stored in ethanol |

### 5.2.4. Adsorption experiments

The FMN were dried at 60 °C in nitrogen atmosphere for about 24 hours and then washed in octane one time for another 24 hours under stirring. Both particles modified in toluene and xylene were later dried and weighed to be used for adsorption of the model NA, which was HBA, in octane shown in Figure 5.3. The model NA varied in concentration from 0.01 to 1.9 g/L HBA. A total of 8 concentration points were measured. The weighed particles were suspended in the model solutions and left under stirring for 24 hours. The solutions were later subjected to a UV-vis measurement (wavelength interval of 200-400 nm) to determine the equilibrium concentrations of the model NA. A surface concentration curve was plotted using equation 5.1:

$$\Gamma = \frac{V(C_0 - C_e)}{Surface\ area} \tag{5.1}$$

where $\Gamma$ is the surface concentration, $V$ is the volume of sample, $C_0$ is the initial concentration, $C_e$ is the equilibrium concentration and *Surface area* is the total surface area of the particles.

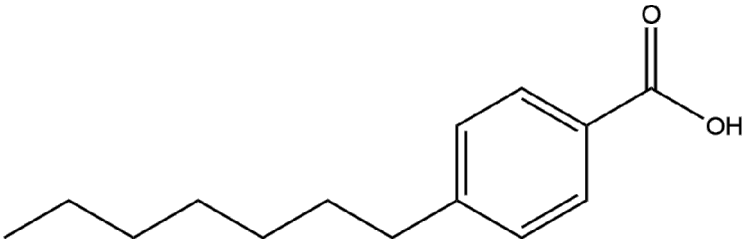


4-Heptylbenzoic acid

***Figure 5.3****: Structure of 4-heptylbenzoic acid (HBA).*

### 5.2.5. Particle recycling

The FMN were used for adsorption of the model NA. After that, the particles were removed from the solutions with a magnet. The separated particles were preserved in octane to be used for further adsorptions. A recycling procedure was developed.

The particles were diluted in octane (about 100 mL) and propylamine (60 µL) was added to remove the adsorbed NA. The solution was shaken for 24 hours. The particles were washed in octane and shaken for 24 hours, then the particles were dried at 60 °C under nitrogen. The dried particles were then tested for adsorption capacity as described in Chapter 5.2.4.

Assuming that all propylamine takes one HBA molecule from the adsorbed surface of the FMN, amount of needed propylamine can be calculated from the equation 5.2.

$$\sum_{n} \frac{A_{Ti}\Gamma_i M_{PA}}{M_{HBA}} = m_{PA} \tag{5.2}$$

where $A_{Ti}$ is the total area of the particles of concentration point i, $\Gamma_i$ is the surface concentration of the particles of concentration point i, $n$ is number of concentration points, $M_{PA}$ is the molecular weight of propylamine, $M_{HBA}$ is the molecular weight of HBA and $m_{PA}$ is the mass of propylamine needed. When performing the experiment an excess of ten times needed propylamine (60 µL) was used.

## 5.3. Selectivity of amino-functionalized particles

Commercial silica particles with amino (-$NH_2$) groups were tested in a crude oil to see the amino groups selectivity towards NA in a real oil. The crude oil used was an acidic sample from the Heidrun field in the North Sea. A summary of Heidrun crude oil before and afte adsorption is given in Table 6.7.

The Heidrun oil was poured from a jerry can into one-liter bottles after being heated to 60 °C and manually shaken. The crude oil was then centrifuged to remove water. The Isolute $NH_2$ silica particles were rinsed in hexane for 24 hours to clean them for potential contamination and then dried under nitrogen. The rinsed particles (16.19 g) were added to the crude oil (251.72 g) and shaken for 24 hours. The particles were removed by centrifugation (11000 rpm, 10 min). The crude oil sample was then tested with respect to different parameters.

## 5.4. Nanoparticle and crude oil characterization

### 5.4.1. Gas adsorption

The BET method was used to estimate the specific surface area of the different synthesized particles. BET is a multilayered adsorption theory, which can be used to calculate the specific surface (area/mass) from the mass of a sample by measuring the difference in pressure.

The instrument used to determine the specific surface area of the different particles was a TriStar 3000 (Micrometics Instrument Corporation) using TriStar 3000 v6.04 as software. The samples were weighed and degassed. The degassing was carried out at 300 °C and about

200 mTorr for 24 hours. After the degassing, the samples were cooled at room temperature and inserted into sample ports of the TriStar 3000 and then submerged into liquid nitrogen.

### 5.4.2. Total acid number

To know the amount of acids adsorbed onto the silica particles from the Heidrun crude oil, TAN of the crude oil was determined before and after the silica particle adsorption. The TAN determination method was a non-aqueous acid-base titration used to determine the molar amount of acids in an organic solvent, usually a crude oil. The titration reaction is given in equation 5.3 and the electric potential is the parameter that changes to determine the inflection point of the titration:

$$\text{TBA-OH+R-COOH-}\rightarrow\text{TBA-OOC-R+}H_2O \tag{5.3}$$

where TBA is tetrabutyl-ammonium hydroxide. Knowing the concentration of TBA, mass of oil and the volume of TBA used to reach infliction point, TAN can be determined by equation 5.4:

$$TAN = \frac{M_{KOH} C V_{eq}}{m_{Oil}} \tag{5.4}$$

where $M_{KOH}$ is the molecular weight of potassium hydroxide, $C$ is the concentration of titrant, $V_{eq}$ is the volume of titrant added until the infliction point, and $m_{oil}$ is the mass of crude oil. The TAN values are determined according to the D664-95 ASTM method [53].

### 5.4.3. Electron microscopy

TEM was used to get an image of the synthesized particles. From these images, an idea of size, shape and the particles tendency to flocculate could be obtained. Naked (metal core), silica-coated and amino-functionalized particles were subjected to the analysis.

TEM is a microscopy technique, which uses a beam of electrons to be transmitted through a thin film of specimen. The basic principle of TEM uses the fact that electrons de Broglie wavelength is much smaller than the wavelength of visual light, and can therefore acquire a higher resolution than an ordinary microscope.

The TEM work was carried out on the NORTEM JEOL JEM-2100F instrument with a field emission gun (FEG) operated at 200kV, at the TEM Gemini Centre, Norwegian University of Science and Technology (NTNU).

### 5.4.4. Elemental analysis

An elemental analysis was performed on the crude oil before and after adsorption with commercial nanoparticles, and also on the amino-functionalized nanoparticles. For the synthesized amino-functionalized nanoparticles the analysis was used to determine if the functionalization reaction had been successful (presence of amino-functions). The crude oil was tested to see what amount of species was adsorbed by the commercial nanoparticles. The analysis was performed by the laboratory SGS Multilab (Evry, France). Carbon (C), hydrogen (H) and nitrogen (N) concentrations were determined by thermal conductivity, and oxygen (O) and sulfur (S) by infrared measurements.

### 5.4.5. Fourier transform infrared spectroscopy

Fourier transform infrared spectroscopy (FTIR) is a technique where an infrared spectrum of a solid or liquid is obtained. It is called Fourier Transform because of the mathematical method that is used for simplified handling of data. This technique measures the absorption of infrared radiation by the investigated material versus wavelength. The infrared absorption bands identify molecular components and structures. When a material is irradiated with infrared radiation, absorbed IR radiation usually excites molecules into a higher vibrational state. The wavelength of light absorbed by a particular molecule is a function of the energy difference between the at-rest and excited vibrational states. The wavelengths that are absorbed by the sample are characteristic of its molecular structure.

The FTIR tests were performed on all the different types of synthesized nanopartivcles and commercial $NH_2$ particles as well as on the crude oil before and after the adsorption. FTIR spectra were recorded using IR spectrophotometer Tensor 27, from Bruker, using OPUS as the software, with a wavelength interval of 500 $cm^{-1}$ 4000 $cm^{-1}$.

### 5.4.6. Asphaltene precipitation

Asphaltene precipitation is a method were crude oil is diluted in low carbon number aliphatic component, since asphaltene is not soluble in these components they can be separated through filtration.

The asphaltene concentration of the crude oil were measured with this method before and after silica particles adsorption were performed. Crude oil (ca. 4 g) was mixed with hexane (ca. 160 mL) and stirred for 24 hours. The solution was then filtrated through a filter (Millipore 0.45 μm). The residue from the filter was dried in nitrogen for 24 hours and then weighed. From this the asphaltene concentration was calculated.

### 5.4.7. Ultraviolet-visible spectroscopy

UV-vis spectroscopy was performed on the crude oil before and after the adsorption to detect any potential change in the absorption spectra. Since most of the naphthenic acids in crude oils are aliphatic, a change would indicate that a molecule with a conjugated system had been adsorbed. It was also used to determine the concentration change in a model naphthenic acid before and after adsorption onto functionalized magnetic particles.

In UV-vis spectroscopy, electromagnetic wave in the wave region, 200-800 nm is passed through a sample. The sample absorbs the light with the wavelength corresponding to the excitation energy in the specific molecule. The measured absorbed light can then be found using the Beer-Lambert –Law, equation 5.5:

$$Ab = \log(\frac{I_0}{I}) = \varepsilon C l \tag{5.5}$$

where $Ab$ is absorbance, $I_0$ and $I$ is the intensity at a given wavelength before and after going through the sample, $l$ is the path length through the sample, $\varepsilon$ is the molar absorptivity and $C$ is the concentration. In organic materials, conjugated systems may exhibit electrons excited in the UV-vis wavelength region, while aliphatic molecules do not. UV-vis can therefore be used as a method to see concentration changes in conjugated systems. The instrument used for the measurement was UV-2401PC, Shimadzu.

### 5.4.8. Quartz crystal microbalance

Quartz crystal microbalance (QCM) is a method for determination of a mass variation per unit area by measuring the change in frequency of a quartz crystal resonator. The method was, in this thesis case, used for adsorption experiments to determine the adsorption of the model NA onto functionalized silica surfaces. The experiments were performed with a Q-sense E1 quartz crystal microbalance with simultaneous frequency and dissipation monitoring, mounted with a sensor crystal (Q-Sense Sensor QSX 303 $SiO_2$) with a top layer of silica.The silica sensors

were functionalized with amino groups according to the previously described procedure in chapter 5.2.3 (toluene method).

In a typical experiment a stable baseline of the solvent (octane) was established before injecting a continuous flow of NA in octane solution. After the frequency shift stabilized on the QCM-D, pure octane was washed over the crystal to ensure that the material was properly adsorbed. All surfaces were cleaned according to a standard protocol for silica surface before use. All QCM experiments were performed at 20 °C.

If the dissipation is low (<1E-6), it indicates a stiff monolayer adsorption. Since the low dissipation indicates adsorption as a compact monolayer adsorption, the Sauerbrey equation can be used to calculate the adsorbed mass:

$$\Delta f = -\frac{2 f_0^2}{\rho_Q \upsilon_Q} \frac{\Delta m}{A} \tag{5.6}$$

where $\Delta f$ is the frequency change, $f_0$ is the resonance frequency, $\rho_q$ is the crystal density, $\upsilon_q$ is the shear velocity of the crystal, $\Delta m$ is the change in mass and $A$ is the area of the crystal.

# 6. Results and discussion

## 6.1. Selectivity of amino-functionalized particles

Adsorption selectivity of commercial silica-coated particles towards NA present in Heidrun crude oil was checked in order to verify that no other crude oil compounds are removed during the adsorption procedure.

### 6.1.1. Total acid number

The silica particles exchange capacity (PEC) was given as 0.51 mmol/g and the TAN of the crude oil was measured as 1.7 $mg_{KOH}/g_{oil}$. The amount of particles needed to adsorb all the NA from the crude oil can then be calculated by equation 6.1, assuming that the particles are 100 % selective towards the NA:

$$\frac{TAN}{PEC} = \frac{1.7}{0.51}\frac{mg_{KOH}\,g_{particles}}{g_{Oil}\,mmole_{adsorbant}} = \frac{1.7}{0.51*56.1}\frac{g_{particles}}{g_{Oil}} = 0.059 \qquad (6.1)$$

where *PEC* is the particle exchange capacity. Isolute $NH_2$ particles (16.19 g) was added to crude oil (251.72 g) and shaken for 24 hours to allow adsorption of the naphthenic acids. After the particles were removed by centrifugation the treated crude oil was tested with respect to different parameters.

The concentration of the titrant was found to be $9.20*10^{-2}$ mole/L using equation A.1. The two parallels and standard deviation for the titrant concentration are given in Appendix Table A.1.

The three paralells of measured TAN of the Heidrun crude oil before and after addition of $NH_2$ Isolute particles are given in Table 6.1.

***Table 6.1:*** *TAN adsorption parallels.*

| Heidrun crude oil | Volume titrant (mL) | Mass of oil (g) | TAN ($mg_{KOH}/g_{oil}$) |
|---|---|---|---|
| Before adsorption P.1 | 3.34 | 10.1 | 1.71 |
| Before adsorption P.2 | 3.35 | 10.1 | 1.71 |
| Before adsorption P.3 | 4.20 | 12.8 | 1.69 |
| After adsorption P.1 | 0.40 | 16.0 | 0.13 |
| After adsorption P.2 | 1.29 | 51.1 | 0.13 |
| After adsorption P.3 | 0.60 | 22.4 | 0.14 |

The average TAN of Heidrun crude oil before adsorption was 1.70 $mg_{KOH}/g_{oil}$, with a relative standard deviation from the average of $2.63*10^{-1}$ %. The average TAN after adsorption was the $1.33*10^{-1}$ $mgKOH/g_{oil}$, with a relative standard deviation from the average of 2.02 %. This gives a reduction of 92.2 % in TAN, with a relative standard deviation from the average of $1.78*10^{-1}$ %. This confirms that a major part of crude oil acidic components was removed.

### 6.1.2. Elemental Analysis

An elemental analysis was performed to the crude oil before and after adsorption to see what amount of various species was possibly adsorbed by the commercial nanoparticles. Carbon (C), hydrogen (H) and nitrogen (N) concentrations were determined by thermal conductivity, and oxygen (O) and sulfur (S) by infrared measurements on Heidrun samples before and after the adsorption. The results are presented in Table 6.2.

***Table 6.2.*** *Concentration of elements in crude oil before and after adsorption.*

| Element | Before adsorption (wt%) | After adsorption (wt%) | Relative change (%) |
|---|---|---|---|
| Carbon (C) | 86.3 | 86.7 | 0.46 |
| Oxygen (O) | 0.39 | 0.28 | -28.2 |
| Hydrogen (H) | 12.7 | 12.8 | 1.11 |
| Sulfur (S) | 0.39 | 0.39 | 0.00 |
| Nitrogen (N) | 0,09 | 0.08 | -11.1 |

No big change in concentrations of carbon, hydrogen, and sulfur was registered. The concentration of oxygen went down by 28.2 %, some of which could be attributed to carboxyl groups in NA because of the reduction in TAN.

### 6.1.3. Fourier transform infrared spectroscopy

Functional groups identified in the FTIR spectra are given in Table 6.3 [31].

***Table 6.3:*** *Functional groups of IR spectra [31].*

| Peak | Wavelength ($cm^{-1}$) | Mode of vibration | Functional group |
|---|---|---|---|
| P1 and P2 | 729 and 813 | C-H bending | CH of substituted benzene |
| P3 | 1378 | C-H sym. def. | -$CH_2$ of saturate |
| P4 | 1459 | C-H deformation | -$CH_2$ and -$CH_3$ of saturate |
| P5 | 2854 | C-H stretching | -$CH_2$ and -$CH_3$ of saturate |
| P6 | 2921 | C-H stretching | -$CH_2$ and -$CH_3$ of saturate |

The method was used to visualize a change in concentrations of Heidrun components before and after adsorption Figure 6.1. The structure is preserved. No major changes of the CH bonding or other functions were observed.

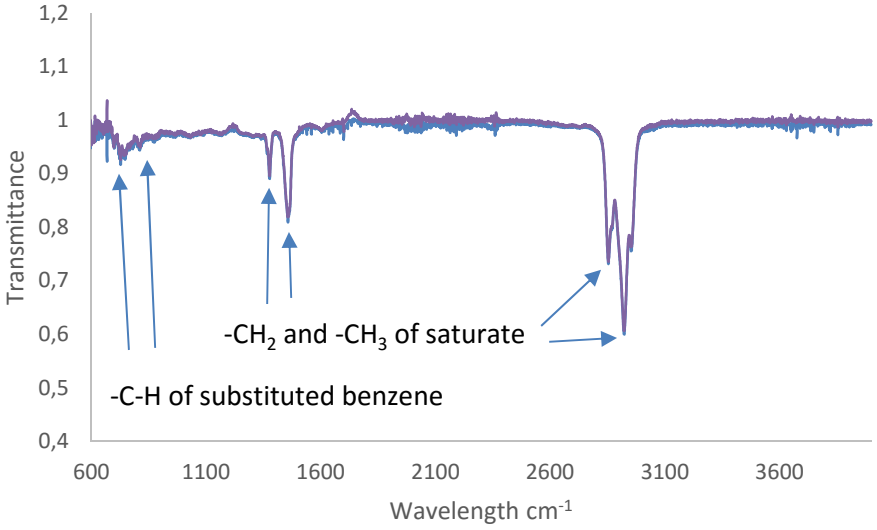


***Figure 6.1:*** *FTIR spectra of Heidrun crude oil before (blue line) and after (purple line) treatment with nanoparticles.*

### 6.1.4. Asphaltene precipitation

The asphaltenes present in crude oils are generally comprised of acidic and basic components [54]. So-called acidic asphaltenes contain acidic groups and may, therefore be partly removed from crude oils together with NA.

The asphaltene concentrations before adsorption and after adsorption measured is given in Table 6.4.

***Table 6.4:*** *Asphaltene concentration in Heidrun crude oil before and after adsorption.*

| Heidrun crude | Mass of crude (g) | Mass of asphaltenes (g) | Asphaltene percentage mass basis (%) |
|---|---|---|---|
| Before adsorption P.1 | 4.03 | 1.87 | $5.11*10^{-1}$ |
| Before adsorption P.2 | 4.06 | 2.08 | $4.82*10^{-1}$ |
| After adsorption P.1 | 4.00 | 1.90 | $3.53*10^{-1}$ |
| After adsorption P.2 | 4.04 | 1.86 | $3.47*10^{-1}$ |

The average asphaltene concentration on a mass basis of Heidrun crude oil before adsorption was $4.97*10^{-1}$ %, with a relative standard deviation from the average of 2.83 %. The average asphaltene concentration on a mass basis of Heidrun crude oil after adsorption was $3.50*10^{-1}$, with a relative standard deviation from the average of $8.53*10^{-1}$ %. This gives a reduction of 29.6 % in asphaltene concentration on a mass basis with a relative standard deviation from the average of 3.50 %. This indicates some asphaltenes has been adsorbed to the Isolute $NH_2$ surface.

### 6.1.5. Ultraviolet-visible spectroscopy

In Figure 6.2 absorbance of different concentrations of Heidrun crude oil over a wavelength interval (200-400 nm) are given. The shape of the wavelength curve changes after adsorption as can be seen Figure 6.2. At about 212 nm after adsorption curves seems to dip more than the pre adsorptions curve. This indicates that there is a difference in adsorption of molecules in the crude oil which both have a conjugated system.

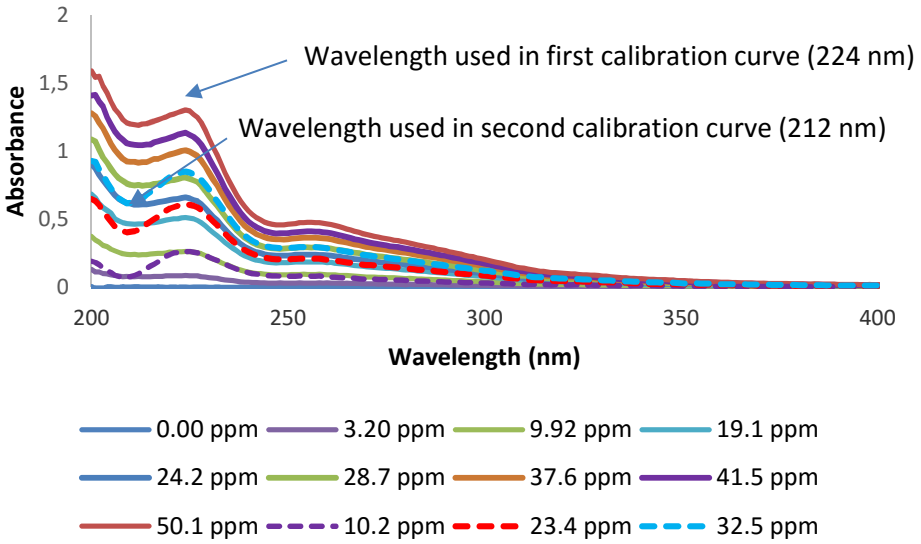


***Figure 6.2:*** *Absorbance at different wavelengths. The full lines are different concentrations of Heidrun crude oil before adsorption. The dashed lines are different concentrations of Heidrun crude oil after adsorption.*

Normalized absorbance spectra around 256 nm are given in Figure 6.3. The spectra seems to be superimposed before and after adsorption for all wavelength except around 224 nm and especially around 212 nm.

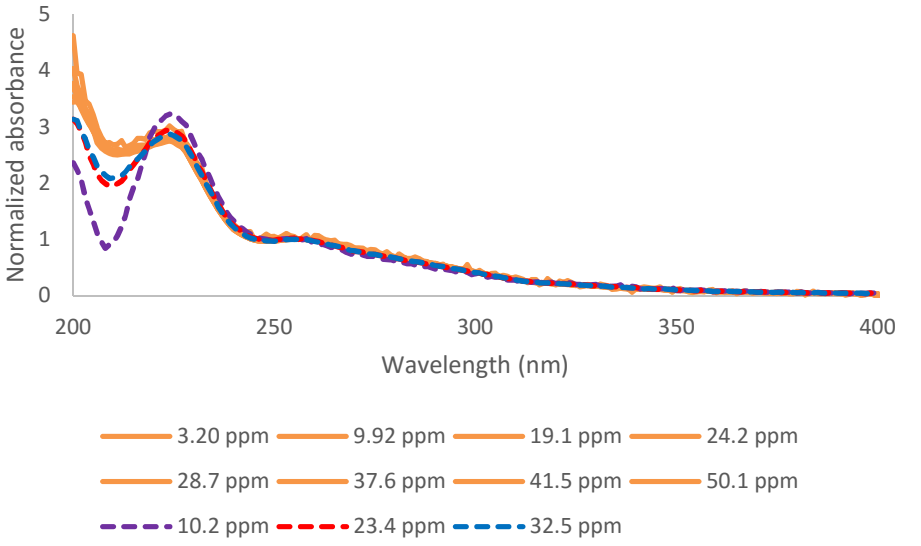


***Figure 6.3:*** *Normalized absorbance spectra around 256 nm. The orange full lines are spectra before adsorption. The dashed line are spectra after adsorption.*

The calibration UV-vis curves for the Heidrun crude oil for both 224 nm and 212 nm are presented in Figure A.1.

From the calibration curve at 224 in Figure A.1 a linear regression was made correlating absorbance to concentration and is given equation 6.2:

$$C = 37.473A - 0.2219 \tag{6.2}$$

where $C$ (ppm) is the concentration and $A$ is the absorbance.

Difference in concentration from UV-vis measurement at 224 nm and the weighed out concentration is given in Table 6.5

***Table 6.5:*** *Concentration change from UV-vis measurement at 224 nm.*

| Parallel | Weighed out concentration (ppm) | UV-vis concentration (ppm) | Relative change (%) |
|---|---|---|---|
| 1 | 23.4 | 22.6 | 3.26 |
| 2 | 32.5 | 31.7 | 2.53 |
| 3 | 10.2 | 9.62 | 5.21 |

From the wavelength at 224 an average concentration change of 3.67 % with a relative standard deviation from the average of 17.8 % was found.

From the calibration curve at 212 nm given in Appendix A.1 a linear regression was made correlating absorbance to concentration and is given equation 6.3:

$$C = 40.902A - 0.2328 \tag{6.3}$$

where $C$ (ppm) is the concentration and $A$ is the absorbance.

Difference in concentration from UV-vis measurement at 212 nm and the weighed out concentration is given in Table 6.6.

***Table 6.6:*** *Concentration change from UV-vis measurement at 212 nm.*

| Parallel | Weighed out concentration (ppm) | UV-vis concentration (ppm) | Relative change (%) |
|---|---|---|---|
| 1 | 23.4 | 17.1 | 27.0 |
| 2 | 32.5 | 25.9 | 20.4 |
| 3 | 10.2 | 4.12 | 59.4 |

From the wavelength at 212 nm an average concentration change of 35.6 % with a relative standard deviation from the average of 27.7 % was found.

A summary of the Heidrun crude oil characteristics before and after adsorption is given in Table 6.7.

***Table 6.7:*** *Summary of crude oil features before and after concentration. Uncertainties given are relative standard deviations from the average, except for elemental analysis of oxygen.*

| **Feature** | **Crude oil before adsorption** | **Crude oil after adsorption** |
|---|---|---|
| TAN ($mg_{KOH}/g_{oil}$) | $1.70 \pm 2.63*10^{-1}$ % | $1.33*10^{-1} \pm 2.02$ %. |
| Water content (ppm) | - | $14 \pm 23$ % |
| Asphaltene concentration (wt %) | $4.97*10^{-1} \pm 2.83$ % | $3.50*10^{-1} \pm 8.53*10^{-1}$ % |
| Oxygen ($g_{Oxygen}/100g_{Oil}$) | $0.39 \pm 2.5$ % | $0.28 \pm 2.5$ % |
| | **Relative changes in crude oil** | |
| Change in TAN concentration (%) | $92.2 \pm 1.78*10^{-1}$ % | |
| Change in asphaltene concentration (%) | $29.6 \pm 3.50$ % | |
| UV-vis ΔC at 224 nm (%) | $3.67 \pm 17.8$ % | |
| UV-vis ΔC at 212 nm (%) | $35.6 \pm 27.7$ % | |
| Mass change in oxygen (%) | 28.2 | |

Selectivity towards adsorption of NA on the Isolute $NH_2$ particles in crude oil seems to be present. Some other components in the crude oil also seem to adsorb, especially asphaltenes, but to a lesser degree than NA.

## 6.2. Synthesis and characterization of magnetic nanoparticles

FMN were synthesized in a procedure involving three separate reactions. First $Fe_3O_4$ particles were synthesized by co-precipitation, secondly the $Fe_3O_4$ particles were silica coated using a sol-gel approach, and finally the $Fe_3O_4/SiO_2$ particles surface were functionalized with APTMS and ODS. A reaction scheme is shown in Figure 6.4.

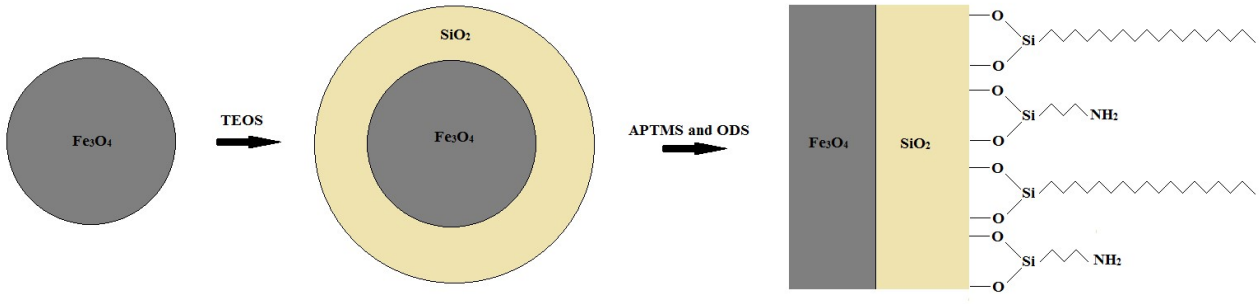


***Figure 6.4:*** *Scheme of reaction. From $Fe_3O_4$ to $Fe_3O_4/SiO_2$ to $Fe_3O_4/SiO_2$ $NH_2/C_{18}$. ODS and APTMS illustrated being grafted onto the silica surface with two anchoring points. This may vary from one to three.*

### 6.2.1. Synthesis of $Fe_3O_4$ particles by co-precipitation

$Fe_3O_4$ nanoparticles were synthesized by co-precipitation reaction. They were stored using three different techniques: dry, in Milli-Q water and in a solution of HCl (0.01 M). The particles stored in the weak solution of HCl showed best separation rates as the acid in this case hindered the cationic changes at the surface of the particles. Figure 6.5. shows appearance of the nanoparticle suspensions 24 hours after preparation. Nanoparticles from the suspension on the right hand side have partly settled to the bottom of the flask, while the other suspension showed no signs of separation. The particles suspended in HCl could be separated with magnetic field much faster than the other ones.

***Figure 6.5:*** *$Fe_3O_4$ naked magnetic nanoparticles in Milli-Q water (left flask) and in a solution of HCl (right flask).*

Figure 6.6. shows separation of the naked $Fe_3O_4$ nanoparticles from solution of HCl (magnet placed under the glass).

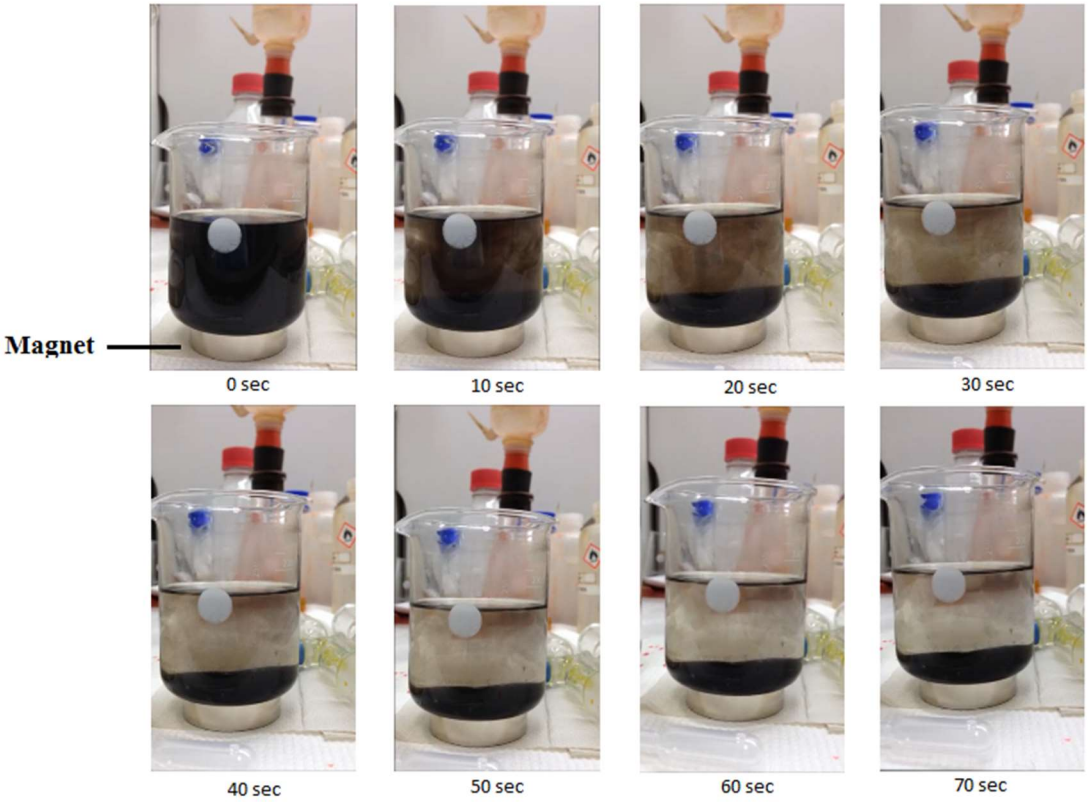


***Figure 6.6.*** *Magnetic separation of $Fe_3O_4$ naked nanoparticles over 70 sec period.*

The technique seems to confirm effective magnetic separation of the particles as the liquid phase is almost clear after 70 seconds.

### 6.2.2. Silica coating of $Fe_3O_4$ particles

After the synthesis silica coating was applied to the surface of the $Fe_3O_4$ particles through a sol-gel approach. The $Fe_3O_4$ particles were activated in an ultra-sonication bath for 25 min. The suspensions were mixed with ethanol, Milli-Q water and aqueous ammonia. TEOS was added under magnetic stirring. The obtained $Fe_3O_4/SiO_2$ particles were stored in a water/ethanol suspension.

### 6.2.3. Surface functionalization of $Fe_3O_4/SiO_2$ particles

$Fe_3O_4/SiO_2$ particles were functionalized with ODS and APTMS in a 1:1 mole ratio by two different methods at 120°C for 8 hours:

- Autoclave experiment using anhydrous toluene (no stirring)
- Reflux experiment using anhydrous xylene in nitrogen atmosphere (magnetic stirring)

After the reactions, particles were washed and stored in pure ethanol.

The second functionalization method was tested as it appears to be simpler compared to the autoclave experiment, which involves high pressure and a solvent (xylene) with boiling point of 138 °C, which is 28 °C higher than for toluene. Also magnetic stirring could be introduced for the second experiment. The two methods were later compared by means of elemental analysis, UV-vis spectroscopy adsorption, specific surface area and TEM.

Figure 6.7. shows dried Fe3O4-1.1, $Fe_3O_4/SiO_2$-1.1and $Fe_3O_4/SiO_2$ $NH_2/C_{18}$ -1.1.1-t. The particles agglomerated in aggregates after drying and it was challenging to break these larger particles during resuspension required for further modifications. That was one of the reasons why it was decides to keep the particles in liquid phase between reactions or during storage. It can be seen form the Figure 6.7. that the particles exhibited a change in color following the modification stages: black, brown and orange respectively for Fe3O4-1.1, $Fe_3O_4/SiO_2$-1.1and $Fe_3O_4/SiO_2$ $NH_2/C_{18}$ -1.1.1-t. Magnetic properties of the particles have been observed to be reduced in the same order, showing strongest magnetism/visually faster separation rates for the naked nanoparticles. This can be explained by increasing thickness of the coating layer protecting the metal core.


***Figure 6.7:*** *Dried magnetic nanoparticles, from left to right: Fe3O4-1.1, $Fe_3O_4/SiO_2$-1.1and $Fe_3O_4/SiO_2$ $NH_2/C_{18}$ -1.1.1-t.*

### 6.2.4. Gas adsorption

The BET measurements were used to estimate the specific surface area of the different particles. The results are given in Table 6.8.

***Table 6.8:*** *Specific surface area of the synthesized nanoparticles.*

| Nanoparticles | Specific surface area ($m^2/g$) |
|---|---|
| $Fe_3O_4$-1 | 99.7 |
| $SiO_2$- $Fe_3O_4$-1.1 | 114 |
| Functionalized $SiO_2$- $Fe_3O_4$-3.3.1-x | 86.9 |
| Functionalized $SiO_2$- $Fe_3O_4$ 3.3.2-t | 94.2 |

It can be seen from Table 6.8 that the specific surface area of the particles follows the following trend:

$SiO_2$- $Fe_3O_4$ > $Fe_3O_4$ > functionalized $SiO_2$- $Fe_3O_4$

Assuming that the particles are perfect spheres and that density of the $Fe_3O_4$ particles is 5.17 g/cm$^3$ [55], an approximation of the average radius can be calculated. The calculation is given by the following equations:

$$A_S = 4\pi r_s^2 \tag{6.4}$$

$$V_S = \frac{4}{3}\pi r_s^3 \tag{6.5}$$

$$m_S = V_S \rho_S \tag{6.6}$$

$$S = \frac{A_S}{V_S} = \frac{3}{r_S \rho_S} \tag{6.7}$$

where $A_s$ is the area of the sphere, $V_s$ is the volume of the sphere, $m_s$ is the mass of the sphere, $S$ is the specific surface area, $r_s$ is the radius of the sphere and $\rho_s$ is the density of the sphere. Solving the last equation for $r_s$ gives an average particle diameter of 11.7 nm. This size is consistent with the TEM images and diffraction pattern analysis from Ronander thesis [1].

Even though the size of the particle increases and a decrease in specific surface area would be expected from equation 6.7, the specific surface area of the coated particles increases by about 14.6 %. This may be explained by a higher degree of porosity in $SiO_2$ than in $Fe_3O_4$. The density of $SiO_2$ is also lower than $Fe_3O_4$, so the contribution in the area/mass ratio is smaller.

After the functionalization reaction, the specific surface area went down. This may be because the surface molecules have blocked some pores in the silica, as illustrated in Figure 6.8 (C).

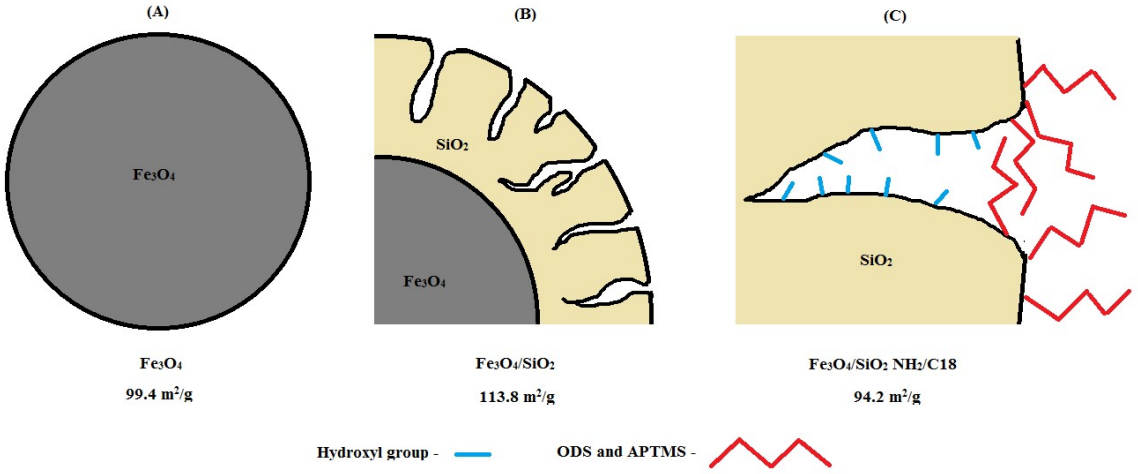


***Figure 6.8:*** *Illustration of possible surface of nanoparticles. (A) Naked $Fe_3O_4$ particle. (B) $Fe_3O_4$ particle coated with porous $SiO_2$ (illustration is not quantitatively representative). (C) Silica pore with surface grafted ODS and APTMS blocking part of the surface.*

### 6.2.5. Fourier transform infrared spectroscopy

The FTIR spectra of $Fe_3O_4$-1. particles, $Fe_3O_4/SiO_2$-1.1. particles, $Fe_3O_4/SiO_2$ $NH_2/C_{18}$ 1.1.1-t and the commercial $NH_2$ particles are given in Figure 6.9.

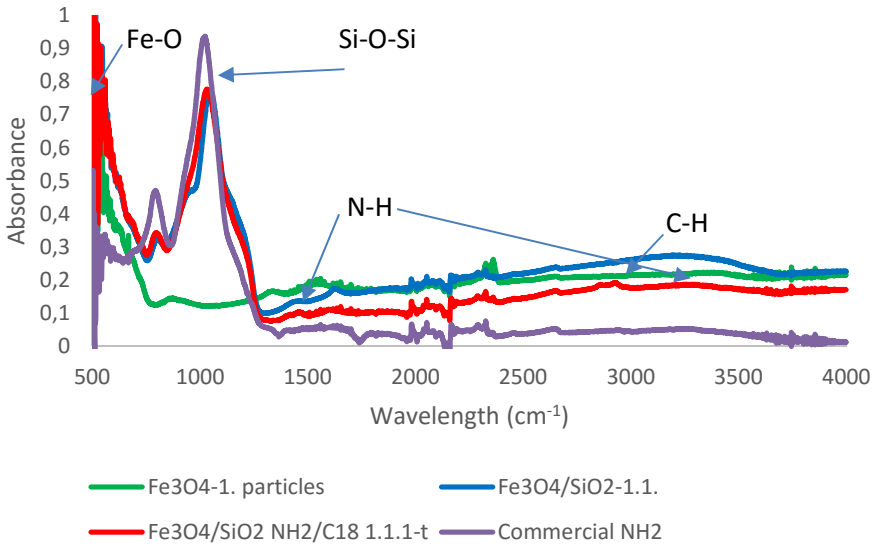


***Figure 6.9:*** *FTIR spectra of $Fe_3O_4$-1. particles, $Fe_3O_4/SiO_2$-1.1. particles, $Fe_3O_4/SiO_2$ $NH_2/C_{18}$ 1.1.1-t and commercial $NH_2$ particles.*

A summary of wavelengths of interest and their respective groups is given in Table 6.9.

***Table 6.9:*** *Functional groups of IR spectra [24].*

| Wavelength ($cm^{-1}$) | Mode of vibration | Functional group |
|---|---|---|
| 560 | - | Fe-O |
| 1080 | - | Si-O-Si |
| 2851 and 2921 | C-H stretching | C-H |
| 1498 and 3361 | N-H stretching and bending | N-H |
| 3420 | - | O-H |

The peak at 560 indicating Fe-O group is present in all particles except the commercial $NH_2$ particles.

Comparing the naked $Fe_3O_4$ particles with the $SiO_2$ particles shows a clear indication that silica has been formed in the coating reaction: the peak at ca. 1080 $cm^{-1}$. Comparing the functionalized particles with the silica-coated and the commercial $NH_2$ particles: the peaks at 2851 and 2921 $cm^{-1}$ may indicate C-H bond and that the $C_{18}$ chains has successfully grafted onto the silica surface. However, this is probably to a very little extent considering results from the elemental analysis. The C-H peak may also be coming from APTMS.

The amino group would be expected to be at 1498 and 3361 $cm^{-1}$ region, but since there is little difference between the silica coated particles and the commercial $NH_2$ particles, it seems that the amino groups do not show up in these spectra. One reason for the weak indication in the IR spectra of amino groups and carbon chain groups on the silica surfaces can be that the instrument is not sensitive enough.

### 6.2.6. Elemental analysis

The results of the elemental analysis on a mass basis of 100 g are given in Table 6.9.

***Table 6.9:*** *Elemental analysis with a mass basis of 100 g.*

| **Element** | **$Fe_3O_4$ 3.3. (g)** | **$Fe_3O_4/SiO_2$ $NH_2/C_{18}$ 3.3.2-t (g)** | **$Fe_3O_4/SiO_2$ $NH_2/C_{18}$ 3.3.1-x (g)** |
|---|---|---|---|
| Hydrogen | 0.51 | 1.04 | 0.98 |
| Carbon | <0.30 | 3.60 | 3.20 |
| Nitrogen | <0.10 | 1.11 | 0.89 |
| Oxygen | 26.42 | 15.5 | 15.0 |
| Sulfur | <0.10 | <0.10 | <0.10 |

In Table 6.10 moles per 100 g particles are summarized.

***Table 6.10:*** *Elemental analysis, moles per 100 g of particles.*

| Element | $Fe_3O_4$ 3.3. (g) | $Fe_3O_4/SiO_2$ $NH_2/C_{18}$ 3.3.2-t (g) | $Fe_3O_4/SiO_2$ $NH_2/C_{18}$ 3.3.1-x (g) | Molecular weight (g/mole) |
|---|---|---|---|---|
| Hydrogen | 0.51 | 1.03 | 0.97 | 1.00 |
| Carbon | 0.00 | 0.30 | 0.27 | 12.0 |
| Nitrogen | 0.00 | 0.08 | 0.06 | 14.0 |
| Oxygen* | 1.65 | 0.97 | 0.94 | 15.9 |
| Sulfur | 0.00 | 0.00 | 0.00 | 32.1 |

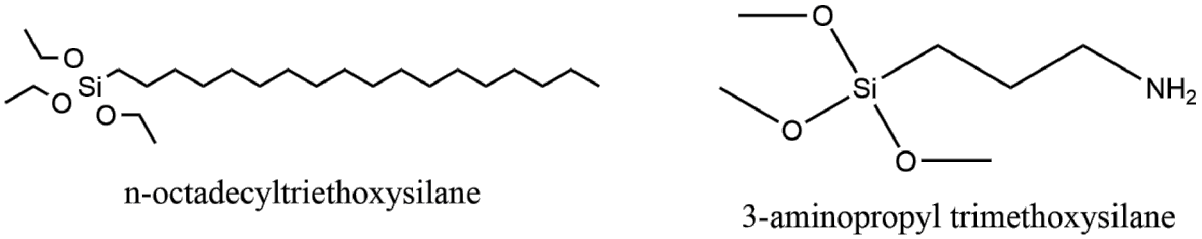


***Figure 6.10:*** *Structure of ODS and APTMS.*

As can be seen from Figure 6.10, the ratio of mole APTMS to mole nitrogen is one to one. Assuming that all the nitrogen in the elemental analysis comes from APTMS, mole of APTMS per gram, can be calculated from equation 6.8:

$$n_{APTMS} = n_N \tag{6.8}$$

where $n_{APTMS}$ is mole APTMS per gram particle and $n_N$ is mole nitrogen per gram particle.

Different reaction possibilities of trimethoxysilanes with a silica surface are given in Figure 6.11, where k is the number of alkoxy groups not reacted with the silica surface. This means that the amount of carbon from one ODS or APTMS molecule will differ depending of the size of k.

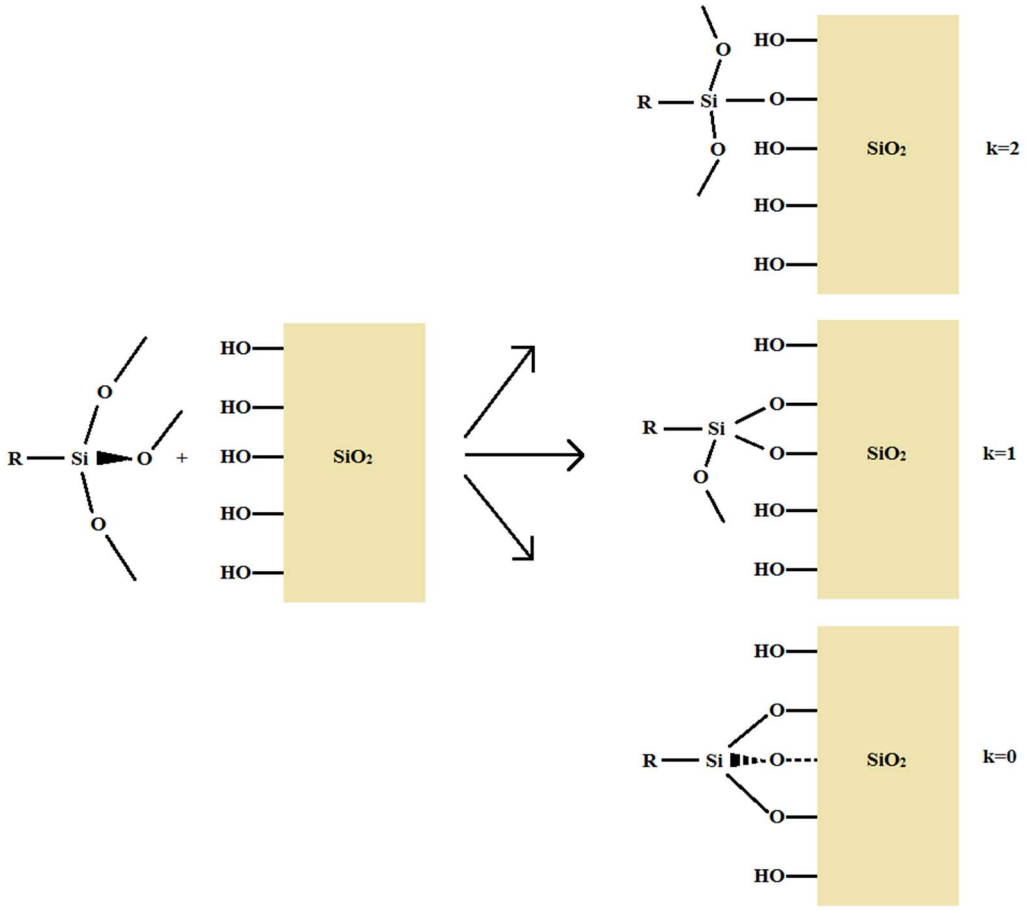


***Figure 6.11:*** *Reaction possibilities of trimethoxysilanes, k is the number of alkoxy groups not reacted with the $SiO_2$ surface.*

Assuming that all the carbon in the elemental analysis is coming from APTMS and ODS, Figure 6.10 and Figure 6.11 are used to find mole ratios in ODS. Mole ODS per gram can be calculated and is given by equation 6.9.

$$n_{ODS} = \frac{(n_C - n_{C-APTMS})}{C_{InODS}} = \frac{(n_C - n_N(3+k))}{(18+2k)} \tag{6.9}$$

where $n_{ODS}$ is mole ODS per gram particle, $C_{InODS}$ is number of carbons in ODS reacted onto the surface, $n_C$ is mole carbon per gram particle, $n_{C\text{-}APTMS}$ is mole carbon per gram coming from the APTMS molecule, and $k$ is the number of alkoxy groups reacted with the silica surface, $k \in [0\text{-}2]$, assuming $k$ is the same for APTMS and ODS.

The total carbon to nitrogen mole ratio for the functionalized particles are 3.78 and 4.19 for the toluene and xylene reactions respectively. In unreacted APTMS, there are six carbons: three in the chain and one in each of the methoxy groups. With a carbon to nitrogen ratio less

than four and assuming all carbon in the elemental analysis stems from ODS or APTMS, at least some of the APTMS molecules are totally grafted onto the surface or in a polymerization reaction. With this low carbon to nitrogen ratio, it leaves very little carbon left accounting for the ODS, which seems to indicate that the grafting of ODS has occurred to a far lesser degree than APTMS.

Assuming that all the hydrogen in the elemental analysis comes from APTMS, ODS and unreacted hydroxyl groups on the silica surface, unreacted hydroxyl groups can be found from equation 6.10:

$$n_H - n_{APTMS}(8+3k) - n_{ODS}(37+k) = n_{-OHur} \tag{6.10}$$

where $n_H$ is mole hydrogen per gram particle and $n_{-OHur}$ is mole unreacted hydroxyl groups per gram particle on the silica surface.

Knowing the specific surface area of the molecules, mole per surface area can be found from equation 6.11:

$$\frac{Specific\ mole}{Specific\ surface\ area} = \frac{mole}{area} \tag{6.11}$$

Mole/$m^2$ for ODS, APTMS and unreacted -OH groups with varying degree of alkoxy groups not reacted is plotted in Figure 6.12. Assuming that ODS and APTMS have the same degree of alkoxy groups not reacted ($k_{ODS}=k_{APTMS}$).

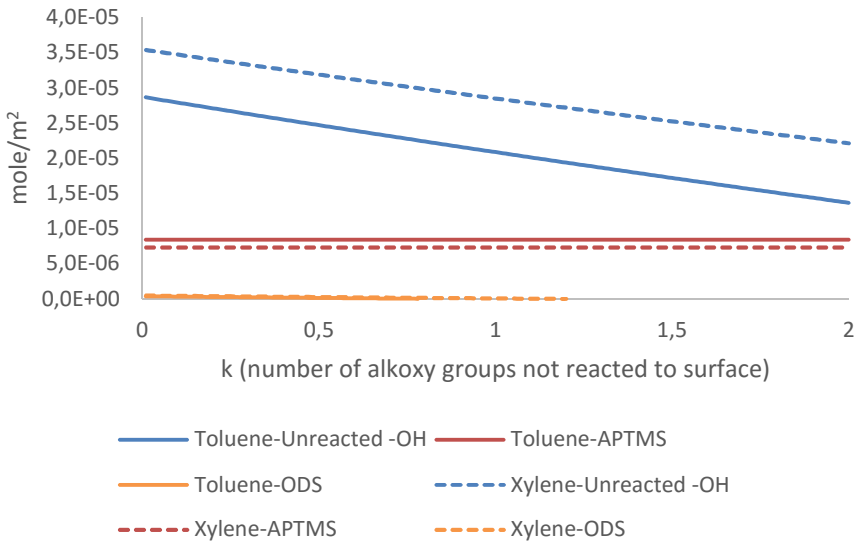


***Figure 6.12:*** *Surface concentration (mole/m2) –OH, APTMS and ODS for varying degree of grafting. k is the number of alkoxy groups not reacted to the $SiO_2$ surface.*

From Figure 6.12, it is obvious that the ODS grafting has occurred to a far lesser degree than APTMS independent of k. Actually it is possible that no ODS has been grafted onto the silica surface. This may be because the amino group on the APTMS molecule is attracted to the silica surface. When the amino group is already adsorbed to the surface it may be a higher probability for the alkoxy groups of the APTMS molecule to react onto the silica surface compared to the ODS alkoxy groups. A possible solution may be to graft the ODS in a separate reaction first, and then graft APTMS.

A summary of mole/g and mole/$m^2$ for the different particles with k=0 and k=2 is given in Table 6.12.

***Table 6.11:*** *Specific mole and surface concentration for functionalized particles with k=0 and k=0.*

| | **$Fe_3O_4/SiO_2$-$NH_2/C_{18}$-3.3.2-t k=0** | **$Fe_3O_4/SiO_2$ $NH_2/C_{18}$-3.3.2-t k=2** | **$Fe_3O_4/SiO_2$ $NH_2/C_{18}$-3.3.1-x k=0** | **$Fe_3O_4/SiO_2$-$NH_2/C_{18}$-3.3.1-x k=2** |
|---|---|---|---|---|
| APTMS (mole/g) | $7.92*10^{-4}$ | $7.92*10^{-4}$ | $6.35*10^{-4}$ | $6.35*10^{-4}$ |
| APTMS (mole/$m^2$) | $8.41*10^{-6}$ | $8.41*10^{-6}$ | $7.31*10^{-6}$ | $7.31*10^{-6}$ |
| ODS (mole/g) | $3.40*10^{-5}$ | 0.00 | $4.17*10^{-5}$ | 0.00 |
| ODS (mole/$m^2$) | $3.60*10^{-7}$ | 0.00 | $4.80*10^{-7}$ | 0.00 |
| -OH (mole/ g) | $2.70*10^{-3}$ | $1.29*10^{-3}$ | $3.08*10^{-3}$ | $1.92*10^{-3}$ |
| -OH (mole/ $m^2$) | $2.86*10^{-5}$ | $1.36*10^{-5}$ | $3.54*10^{-5}$ | $2.21*10^{-5}$ |

Assuming that all reacted alkoxy groups have grafted onto the surface, and that there is no polymerization reaction (an assumption that may not be sound), amount of reacted -OH groups can be found from equation 6.12:

$$(3-k)(n_{APTMS}+n_{ODS})=n_{-OHr} \tag{6.12}$$

where $n_{-OHr}$ is mole of reacted hydroxyl groups per gram particles at the silica surface. In Figure 6.13, percentage of unreacted hydroxyl groups is plotted against degree of alkoxy groups not reacted to the surface.

The Kiselev-Zhuralev [56] constant, 4.6 OH/$nm^2$, gives us the maximum number of -OH groups per nano square meter on amorphous silica, which is $7.65*10^{-5}$ mole OH/$m^2$. Knowing this constant a percentage of hydroxylation of the silica coated surfaces compared to the maximum coverage obtainable, can be found, and is shown in Figure 6.13.

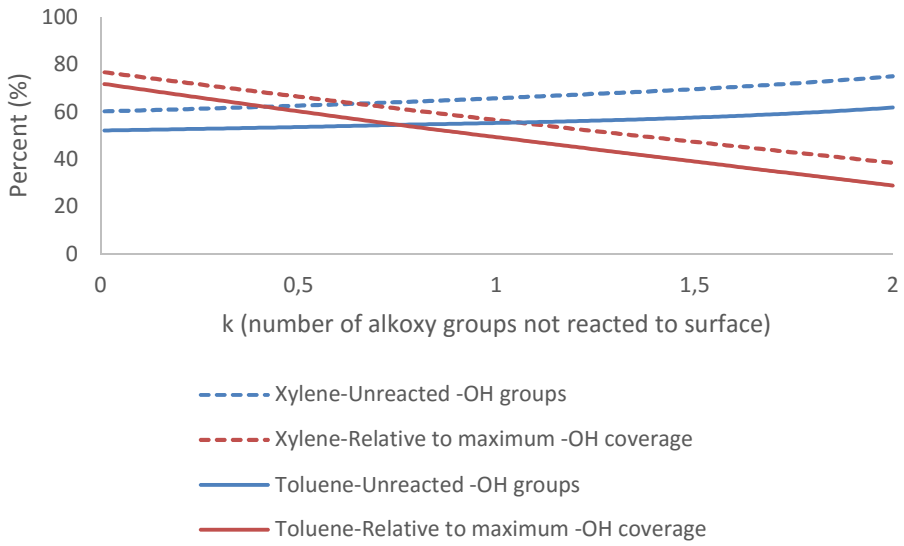


***Figure 6.13:*** *Surface hydroxyl group coverage on silica surface. k is the amount of unreacted alkoxy groups in ODS and APTMS.*

It can be seen from the Figure 6.13. that the -OH coverage on the silica surface is at maximum and the percentage of unreacted -OH is at a minimum when k = 0 (all silanes are grafted). Overall, there seems to be good coverage. A way to increase the mole/$m^2$ of APTMS and ODS may be to prime the silica surface before reaction to maximize the amount of -OH groups on the surface.

### 6.2.7. Transmission electron microscopy

The TEM images of the different particles were recorded and are presented in Figure 6.13-16. The TEM images for the $Fe_3O_4$-3 particles are given in Figure 6.13. The particles seem to have a parallelepiped shape with an affinity to flocculate. In Figure 6.13(D) parallel lines in the particle can be observed indicating the lattices of the atomic structure. From these images it seems that all of the particles are monocrystals. The different direction of the parallel lines in the individual particles is because of the orientation of the particle.

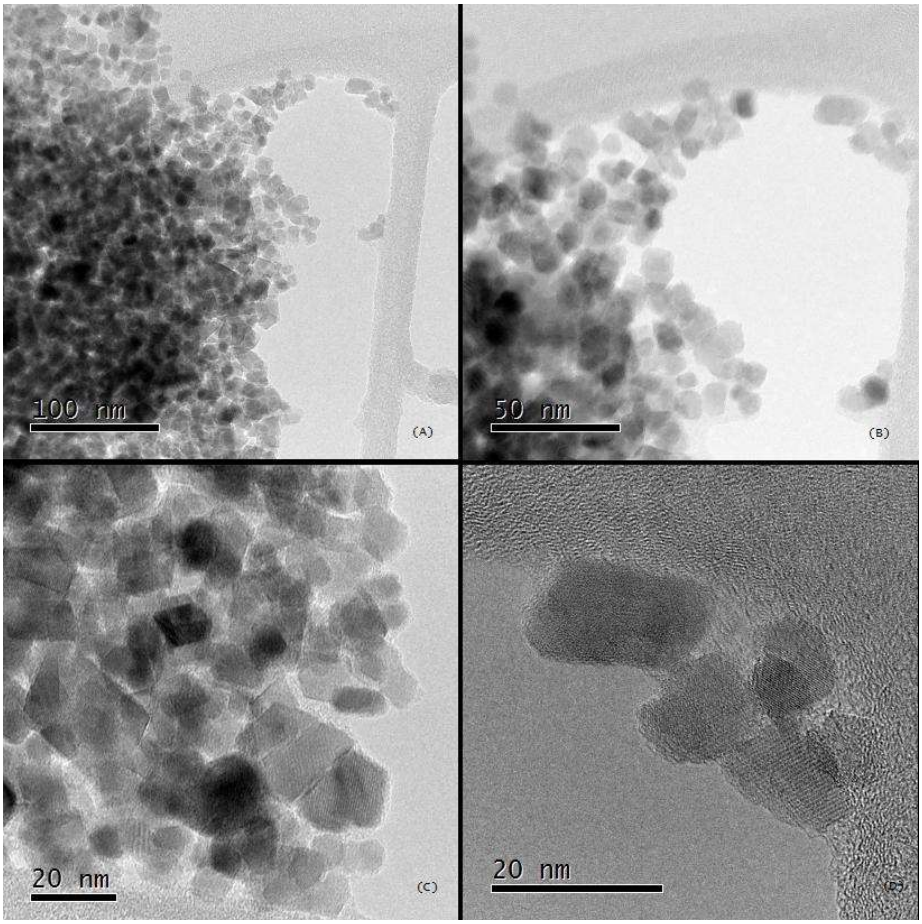


***Figure 6.13:*** *TEM images of* $Fe_3O_4$-3 *particles with different resolutions.*

The size of the $Fe_3O_4$-3 particles in Figure 6.13 seems to be in the range of 10 to 30 nm. This compares well to the BET analysis, where the particle size was calculated to be 11.7 nm (assuming that all the particles have spherical shape). Since spheres is the shape with smallest area to volume ratio, it is expected that the parallelepiped shape would be bigger with the same specific surface area.

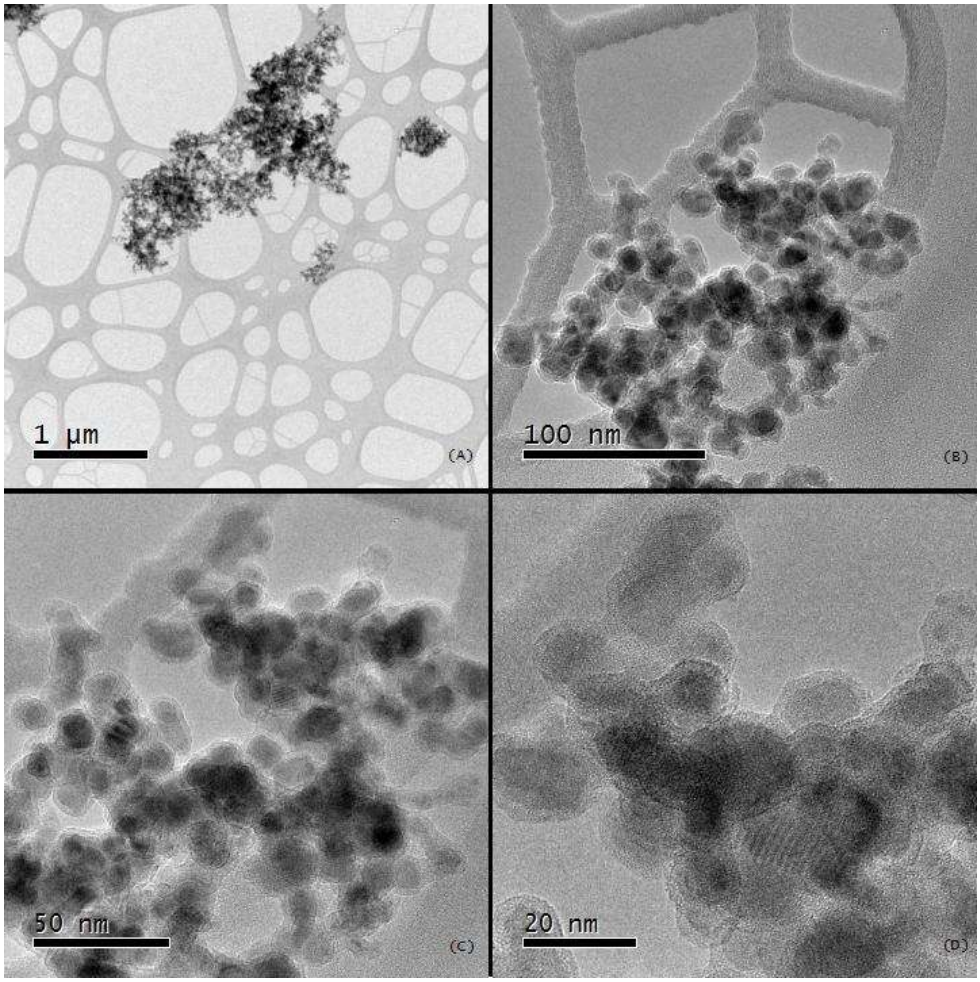


***Figure 6.14:*** *TEM images of* $SiO_2$-Fe3$O_4$-3.3 *particles with different resolutions.*

In the Figure 6.14, the TEM images of $SiO_2$-Fe3$O_4$-3.3 are shown. Through observation it seemed that of all the different particles, the silica coated particles were the ones with the highest degree of flocculation.

In the Figure 6.14 (D), it can be clearly seen that the particles are coated. The coating seems to be amorphous with a crystal core. These results match with XRD analysis given in a previous Master's thesis by Mia Ronander [1].

In the Figures 6.15 and 6.16, the TEM images of $Fe_3O_4/SiO_2$ $NH_2/C_{18}$-3.3.2-t and $Fe_3O_4/SiO_2$ $NH_2/C_{18}$-3.3.1-x are shown. The clustering tendency of these particles seems to be smaller than for the other particles. There was not observed any particular difference between the functionalized particles from the autoclave reaction and the functionalized particles from the xylene reaction. Neither was there observed a visual difference between the silica coated particles and the functionalized particles.

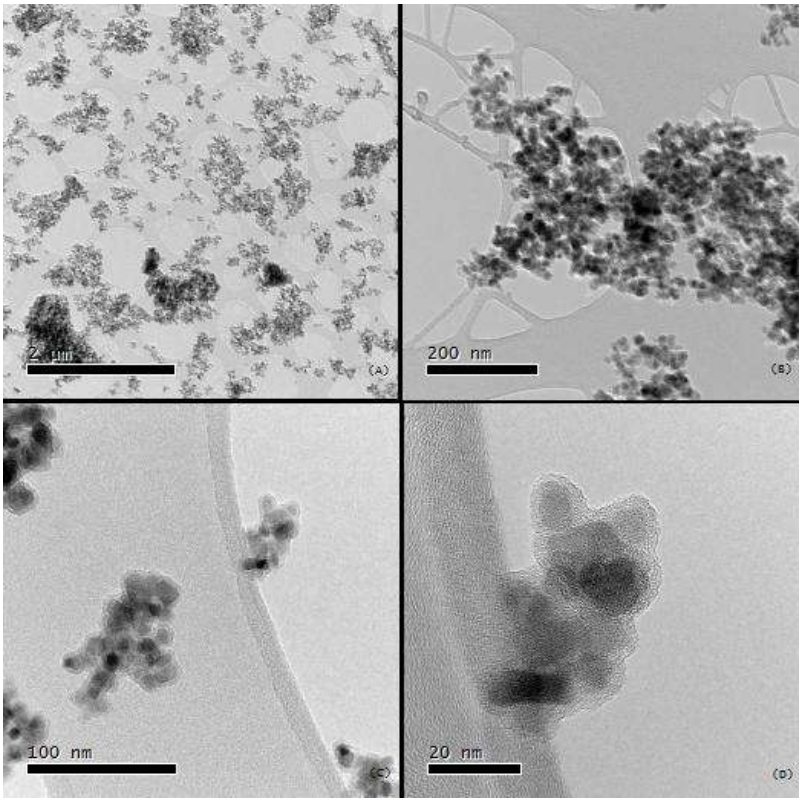


***Figure 6.15:*** *TEM images of* $Fe_3O_4/SiO_2$ $NH_2/C_{18}$-3.3.1-x *particles with different resolutions.*

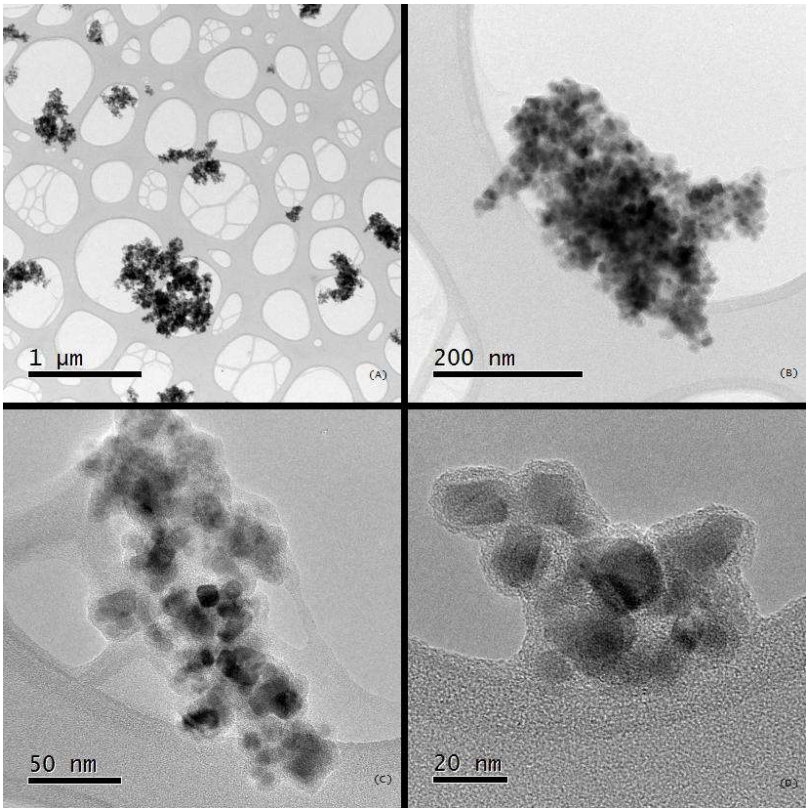


***Figure 6.16:*** *TEM images of* $Fe_3O_4/SiO_2$ $NH_2/C_{18}$*-3.3.2-t particles with different resolutions.*

Figures 6.17 and 6.18 shows size distributions of $Fe_3O_4$-3 and $Fe_3O_4/SiO_2$-3.3 particles respectively. The measurements are done based on Figures A.3 and A.4 included in the Appendix of the thesis. The size distribution seems to have been shifted about 9 nm after the silica coating was applied, which would indicate an average silica coating of ca 4.5 nm. The measurements were taken horizontally and at the particles thickest point. As can be seen from Figure A.3, most of the distinguishable particles lie on the perimeter of the cluster. The biggest particles seem to be in the middle of the cluster. This indicates that the real size of the particles is probably a bit larger. This is supported by the average size calculation in chapter 6.2.4. which was 11.7 nm. Since the particles seem to have a parallelepiped shape, the average size may be better described other than by an average radius.

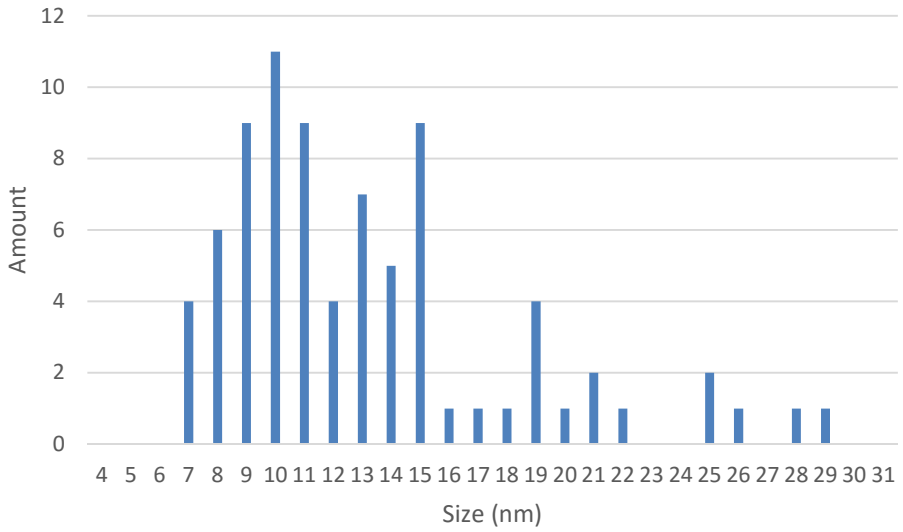


***Figure 6.17:*** *Size distribution of $Fe_3O_4$-3, the measurements were taken horizontally to the picture and at thickest place.*

It is important to note that the results from the size distribution analysis is not very robust, considering the small amount of counted particles (80 for the naked particles and 38 for the silica coated particles).

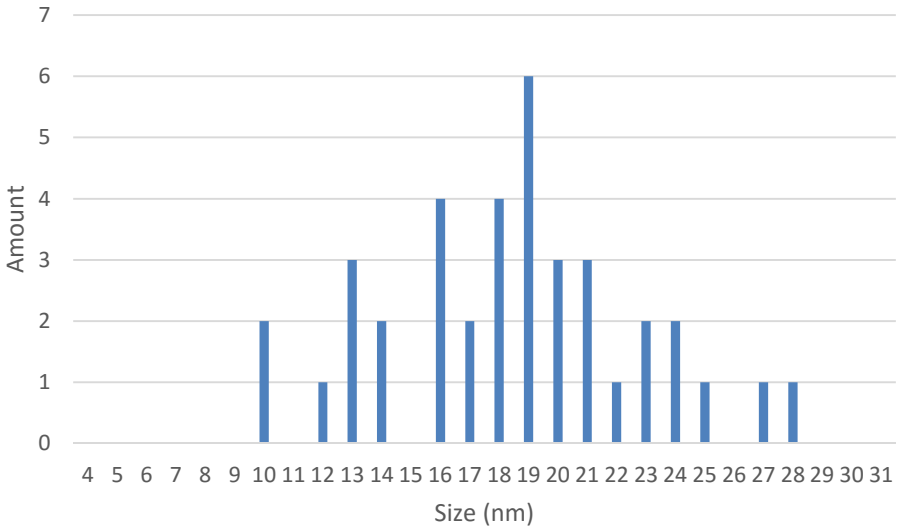


***Figure 6.18:*** *Size distribution of $Fe_3O_4$-$SiO_2$-3.3. The measurements were taken horizontally to the picture and at the particles thickest place.*

A theoretical specific surface area can be calculated from equation 6.13 and 6.14 using sizes obtained from the size distribution analysis (10 nm and 19 nm for $Fe_3O_4$ and $Fe_3O_4/SiO_2$ particles respectively) and assuming them to be spheres.

$$S_{Fe} = \frac{4\pi r_{Fe}^{\ 3}}{\rho_{Fe}\frac{4}{3}\pi r_{Fe}^{\ 3}} = \frac{3}{r_{Fe}} \tag{6.13}$$

$$S_{Si} = \frac{3r_{Si}^{\ 2}}{\rho_{Fe}r_{Fe}^{\ 3} + \rho_{Si}(r_{Si}^{\ 3} - r_{Fe}^{\ 3})} \tag{6.14}$$

where $\rho_{Fe}$ is the density of ironoxide (5.17 g/mL), $\rho_{Si}$ is the density of silica (2.65 g/mL), $r_{Fe}$ is the average radius for the $Fe_3O_4$-3 particles (10 nm), $r_{Si}$ is the average radius for the $Fe_3O_4/SiO_2$-3.3 particles (19 nm), $S_{FeT}$ is the theoretical specific surface area for $Fe_3O_4$-3 particles and $S_{SiT}$ is the theoretical specific surface area for $Fe_3O_4/SiO_2$-3.3 particles. This gives 116 $m^2/g$ and 104 $m^2/g$ for $Fe_3O_4$-3 and $Fe_3O_4/SiO_2$-3.3 particles respectively.

The theoretical specific surface area calculated for $Fe_3O_4$ particles is higher than the measured specific area from BET analysis (99 $m^2/g$). This may be because the size distribution seems to give a smaller size than expected, as discussed earlier. The theoretical specific surface area calculated for $Fe_3O_4/SiO_2$ particles is lower than the measured specific area from BET analysis (114 $m^2/g$). As discussed earlier this may be due to particle porosity. To get an

indication of degree of porosity, a ratio between the measured and the theoretical specific surface area can be calculated form equation 6.15:

$$Ratio = \frac{S_M}{S_T} \tag{6.15}$$

where $S_T$ is the theoretical specific surface area and $S_M$ is the measured specific surface area. The ratios are 0.86 and 1.1 for $Fe_3O_4$ and $Fe_3O_4/SiO_2$ particles respectively, which would indicate that the silica coated particles are a little more porous than the naked particles.

In Figure 6.19, diffraction patterns of the different particles are given. A difference can be seen from the amount of backscatter in the naked particles and the rest of the particles. The backscatter indicates an amorphous structure, which would be the silica in our case.

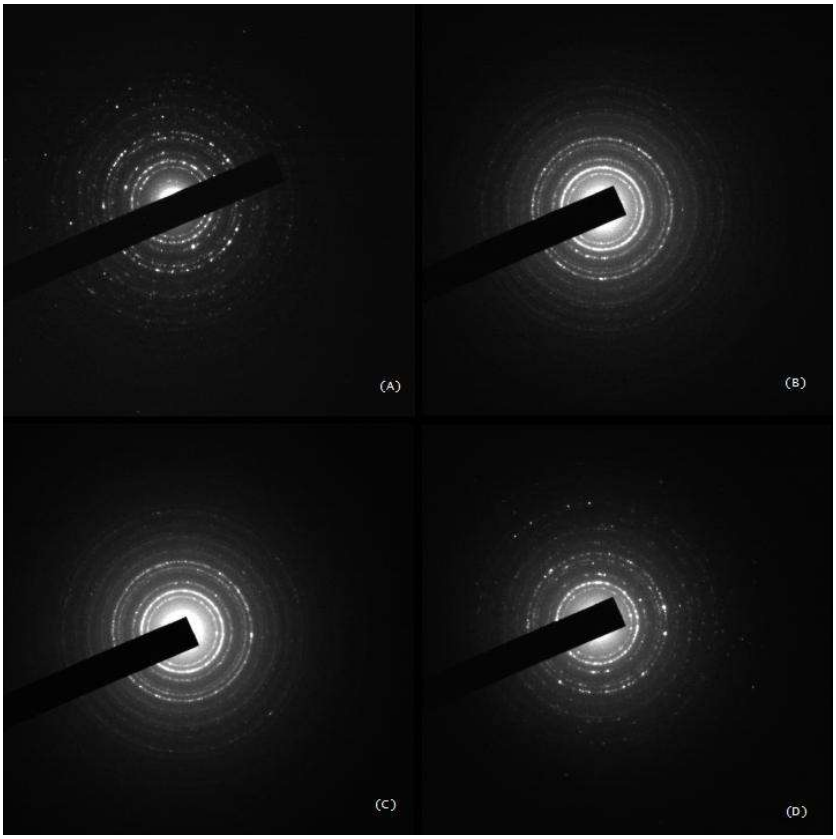


***Figure 6.19:*** *Diffraction patterns of $Fe_3O_4$-3 (A), $Fe_3O_4/SiO_2$-3.3 (B), $Fe_3O_4/SiO_2$ $NH_2/C_{18}$-3.3.1-x (C) and $Fe_3O_4/SiO_2$ $NH_2/C_{18}$-3.3.2-t (D).*

A comparison of lattice spacing form Ronander's XRD analysis [1] and the TEM diffraction images is given in Table 6.12. The lattice spacing values from Ronander's XRD

analysis were found using Braggs law (equation 6.16) and the XRD curve is given in Appendix Figure A.6:

$$n\lambda = 2d\sin(\theta) \tag{6.16}$$

where $\lambda$ is the wavelength, $d$ is the lattice spacing, $\theta$ is the scattering angle, and $n$ is an integer (in this comparision case $n=1$).

The lattice spacing values from the TEM images of $Fe_3O_4$-3 particles were found from Figure A.5. The values given as standard for $Fe_3O_4$ are from [57].

***Table 6.12:*** *Lattice spacing values.*

| **Lattices spacing #** | **Standard $Fe_3O_4$ [57] (Å)** | **$Fe_3O_4$ Ronander [1] (Å)** | **$Fe_3O_4$-3 (Å)** |
|---|---|---|---|
| 1 | 4.85 | - | 4.76 |
| 2 | 2.97 | 2.98 | 2.94 |
| 3 | 2.54 | 2.53 | 2.50 |
| 4 | 2.42 | - | - |
| 5 | 2.11 | 2.09 | 2.06 |
| 6 | 1.71 | 1.70 | 1.69 |
| 7 | 1.62 | 1.61 | 1.61 |
| 8 | 1.48 | 1.48 | 1.47 |
| 9 | 1.28 | 1.27 | 1.30 |
| 10 | 1.09 | - | 1.09 |
| 11 | 0.86 | - | 0.84 |

Lattice spacing values in Table 6.12 are close to each other. The $Fe_3O_4$-3 particles are, therefore, consistent with a magnetite structure. A comparison in intensity and broadness of peaks has not been done.

## 6.3 Adsorption capacity of functionalized nanoparticles

Figure 6.20 gives the absorbance spectra for different concentrations of HBA in octane. From this figure a wavelength of 242 nm was chosen as the wavelength used in the calibration curve. The calibration curve can be found in Figure A.2 in the Appendix. The linear regression equation for the calibration curve is given in equation 6.17:

$$C = 12.71A + 0.4849 \tag{6.17}$$

where $C$ is the concertation in ppm and $A$ is the absorbance. Equation 6.20 was used to find the concentration after adsorption.

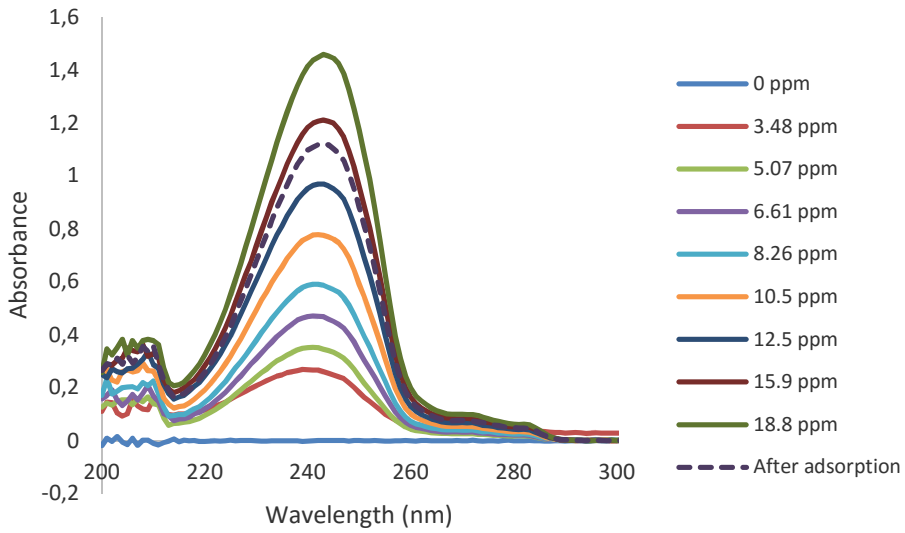


***Figure 6.20:*** *Absorbance spectra of varying concentration. Full lines are used for the calibration curve. The dashed line is one example sample point after adsorption.*

In Figure 6.20 the full lines are before adsorption and the dashed line is after. The shape of the curve does not seem to change after the adsorption.

The surface concentration curves of the FMN and silica coated particles are given in Figure 6.21. The data from the silica coated particles are from Mia Ronander's Master's thesis [1]. The difference in silica surface v1 and v2 are the washing procedure for the particles before adsorption. Where v1 was not washed before adsorption and v2 was washed for 24 hours in octane and then dried before adsorption.

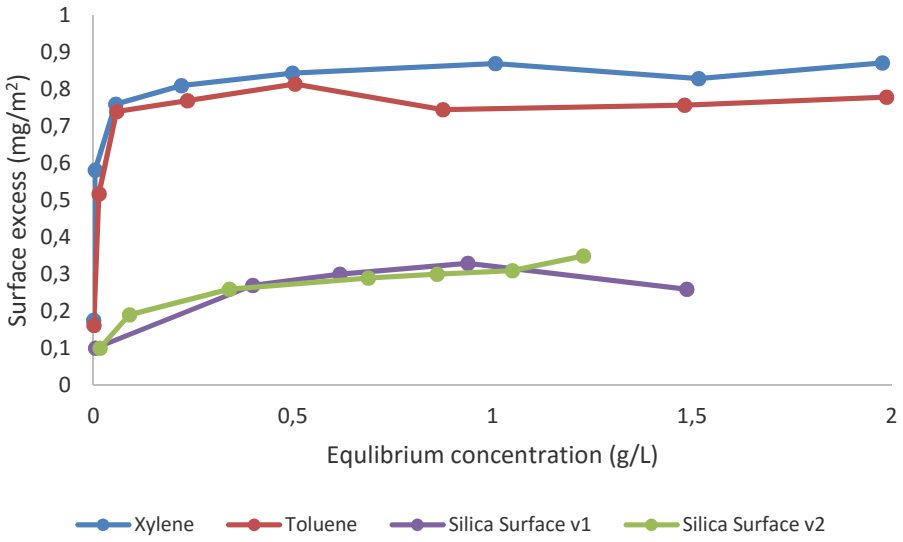


***Figure 6.21:*** *Surface concentration of FMN and silica coated particles.*

Figure 6.21 shows that the functionalization reaction has increased the adsorbed surface concentration. The two functionalization methods revealed similar results for the adsorption of model NA onto the particle surface. The amino-functionalized $Fe_3O_4/SiO_2$ $NH_2/C_{18}$ samples showed 2.7 times higher adsorption capacity compared to the silica-coated $Fe_3O_4/SiO_2$ particles.

The equilibrium surface concentration after the curve has plateaued, which seems to be around 0.5 g/L and given in Table 6.13. The values are an average of all surface concentrations over 0.5 g/L with a relative standard deviation from the average.

***Table 6.13:*** *Average surface concentrations.*

| Particle | Surface concentration ($mg/m^2$) |
|---|---|
| $Fe_3O_4/SiO_2$ $NH_2/C_{18}$-3.3.2-t | $8.54*10^{-1}$ ± 1.05 % |
| $Fe_3O_4/SiO_2$ $NH_2/C_{18}$-3.3.1-x | $7.67*10^{-1}$ ± 1.32 % |
| Silica surface v1[1] | $2.97*10^{-1}$ ± 5.58 % |
| Silica surface v2 [1] | $3.13*10^{-1}$ ± 14.6 % |

### 6.3.1. Quartz crystal microbalance

QCM experiments were performed on amino-functionalized silica sensors using the same procedure as used for the $Fe_3O_4/SiO_2$ particles in toluene solution. The goal was to register a real-time adsorption of the model NA (HBA) onto the surfaces of interest. The QCM experiments were also performed on unmodified silica plates for comparison. The amount of

ODS and APTMS used in the synthesis was the same as for the particles, even though the reaction surface for the sensors and the particles were different. This may give a different kind of coverage for the sensors compared to the particles. In Figure 6.22, a functionalized QCM sensor (Q-Sense Sensor QSX 303 $SiO_2$) is shown. Its surface seems to be heterogeneous. This may be because the sensors were washed with ethanol containing 0.2 % water and during the washing a polymerization reaction of the APTMS and ODS with water may have occurred.

***Figure 6.22:*** *Functionalized QCM sensor.*

Several problems were encountered during the QCM experiments. One example is getting a stable baseline, while there was a flow of octane (0.5 mL/min) over the sensor. The frequency drifted downward, this may indicate a contamination in the octane with a dipole moment, which is being adsorbed onto the sensor's surface. To counteract this behavior, the QCM chamber was filled with octane and the flow was turned off, waiting for an equilibrium between the surface concentration and the solution concentration. In Figure 6.23, the change of frequency in the QCM sensor before equilibrium is shown for three parallels of unmodified surface and functionalized sensors, the QCM chamber is filled with octane and there is no flow.

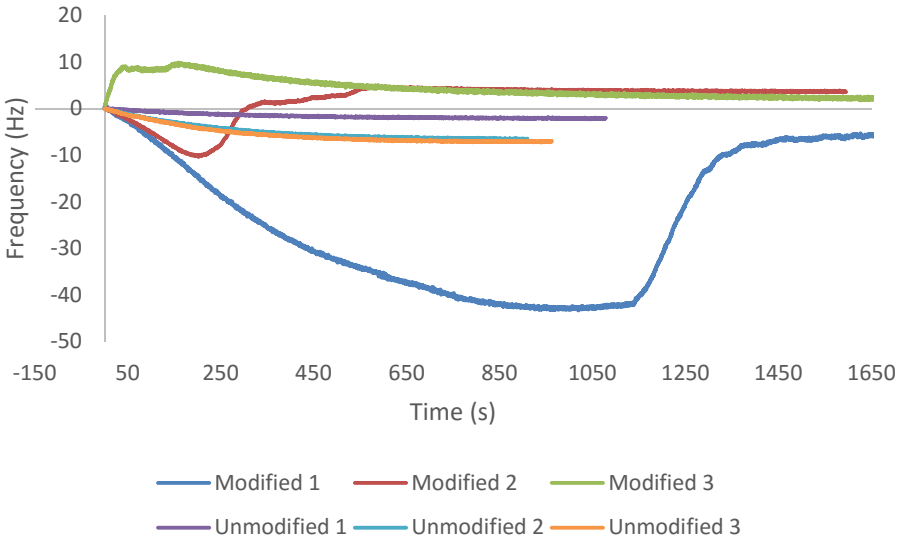


***Figure 6.23:*** *Pre experiment start. Change in frequency over time in QCM sensors before equilibrium*

As can be seen from the Figure 6.23 the modified surfaces differ greatly not only in absolute value, but also in shape. Curve 1 and 2 for the modified sensors may be said to have the same shape, but curve 3 is completely different. A reason for this is hard to explain, but it suggests that the quantitative values of this adsorption experiment should not be used for further experiments. In Figure 6.24 and 6.25, only sensors Modified 2 and Unmodified 2 from Figure 6.23 are shown.

In Figure 6.24 the change in frequency in the QCM sensor over time is shown. The 3$^{rd}$ overtone frequency change and dissipation change was plotted for both the unmodified and modified surface. From 0 to 300 seconds there is octane in the QCM chamber with no flow. At 300 seconds a flow (0.5 mL/min) of 500 ppm HBA in octane starts. At 600 seconds the flow stops and octane flow (0.5 mL/min) starts.

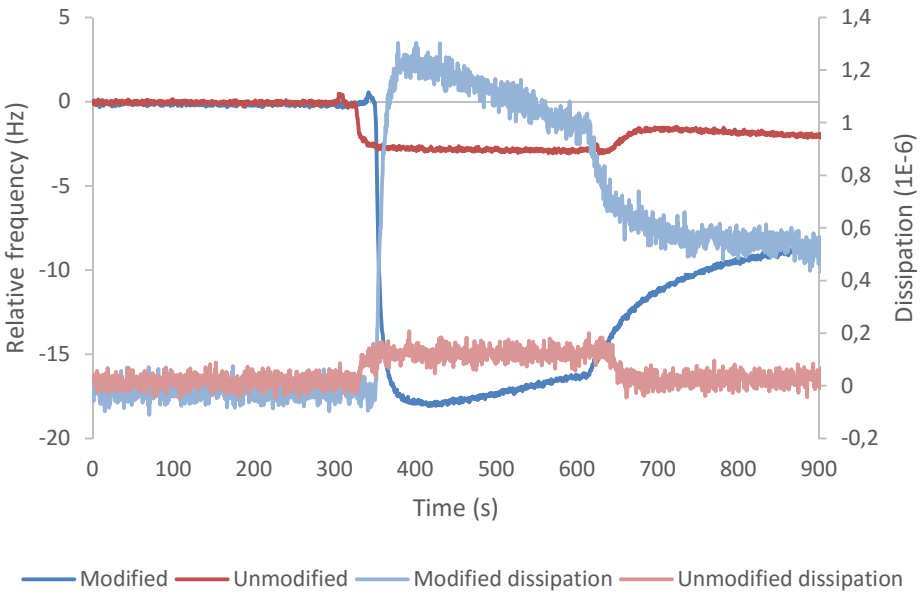


***Figure 6.24:*** *Change in frequency and dissipation over time for the 3rd overtone.*

Since the dissipation energy is smaller than $10^{-6}$ we assume that the adsorbed layer is rigid, and the Sauerbrey equation 5.6 therefore apply.

Using the Saurbrey equation 5.6, a surface concentration over time can be obtained. Surface concentration ($mg/m^2$) over time is given in Figure 6.25.

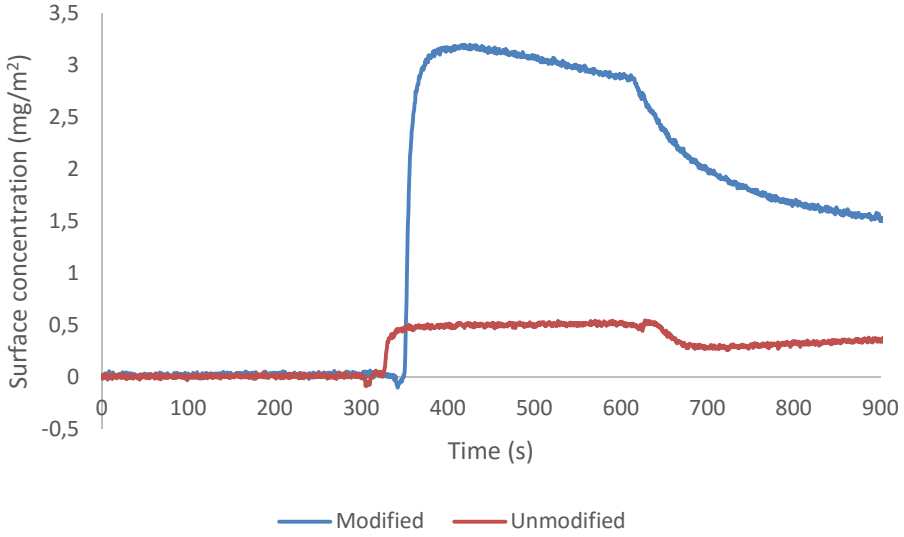


***Figure 6.25:*** *Surface concentration over time.*

The adsorption capacity of the modified sensors compared to the unmodified is about 4.1 times higher as can be seen from the Figure 6.25. This is about the same as was seen from the particles in adsorption experiment, which had a surface concentration difference of a factor

of 2.7. The lower value for the particles may come from a lesser degree of amino group coverage on the FMN compared to the functionalized sensor. From Figure 6.25 it can be seen that the surface concentration at the end of the experiment is 1.5 mg/m$^2$ and 0.37 mg/m$^2$ for the modified and unmodified surfaces respectively. The surface concentration from the adsorption measured with UV-vis was 3.1*10$^{-1}$ mg/m$^2$ and 8.5*10$^{-1}$ mg/m$^2$ for silica coated and FMN respectively. A reason for the lower value for the UV-vis measured surface concentration may be that the QCM experiment all the adsorbed molecules have been measured as compared to the UV-vis measurement, which only measured HBA surface concentration. This also supports the idea that there are some molecules in the octane other than HBA, which adsorb onto the sensor surface. A summary of the surface concentrations found from UV-vis and QCM are given in Table 6.14.

***Table 6.14:*** *Comparison of surface concentration measurement.*

| Method | Concentration (mg/m$^2$) |
|---|---|
| Modified QCM sensor | 1.5 |
| Unmodified QCM sensor | 3.7*10$^{-1}$ |
| Functionalized particles UV-vis | 8.5*10$^{-1}$ |
| Silica coated particles UV-vis | 3.1*10$^{-1}$ |
| Ratio UV-vis measurement (functionalized/silica coating) | 4.1 |
| Ratio QCM measurement (modified/surface) | 2.5 - 2.9 |

Height of the adsorbed layer can be estimated knowing the surface concentration and density of the adsorbed layer. An estimation of 1.01 g/mL is used [58]. The height of the adsorbed layer can give an indication of the orientation of the adsorbed molecule relative to the surface (knowing the length of the adsorbed molecule). This is illustrated in Figure 6.26.

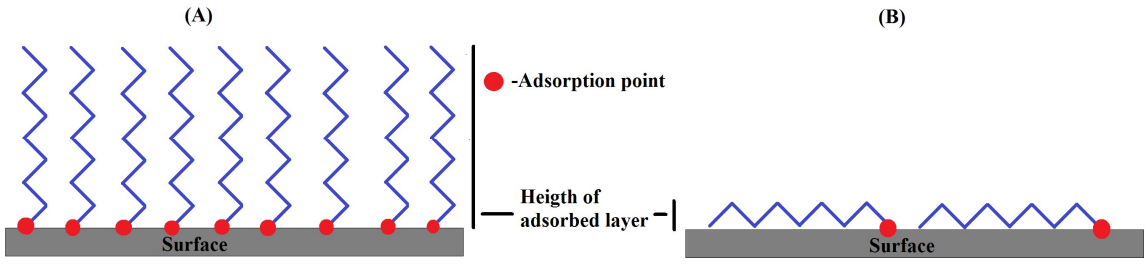


***Figure 6.26:*** *Illustration of molecule tail orientation as a function of height of the adsorbed layer. (A) Max height for adsorbed monolayer, molecules are orthogonal to the adsorbed surface. (B) Adsorbed molecules are parallel to the surface.*

An estimation of the maximum length of HBA molecule can be found using a bond length for C-C of 1.5 Å, a bond angle of 109.5° and estimating 11 C-C bonds in HBA from Figure 5.3. Estimated maximum length of HBA is then 1.6 nm.

In Table 6.15 estimated heights of the adsorbed layer for the different surfaces are given.

***Table 6.15:*** *Estimated heights of the adsorbed layers for the different surfaces.*

| Surface | Height of adsorbed layer (nm) |
|---|---|
| Modified QCM sensor | 0.31 |
| Unmodified QCM sensor | 0.84 |
| Functionalized particles UV-vis | 0.36 |
| Silica coated particles UV-vis | 1.48 |

All heights of adsorbed layers are smaller than the estimated maximum length of HBA molecule.

## 6.4. Particle recycling

A recycling procedure was performed as described in Chapter 5.2., with two parallels for both xylene and toluene particles. The starting concentration of the HBA in octane was 1.898 $g_{HBA}$/L. A summary of the results is given in Table 6.16, where given uncertainties are relative standard deviations from the average.

***Table 6.16:*** *Recycling experiment results. ΔC is the difference in start concentration and equilibrium concentration. Uncertainties given are relative standard deviations from the average.*

| Particle | ΔC (ppm) | Surface concentration (mg/m$^2$) |
|---|---|---|
| $Fe_3O_4/SiO_2$ $NH_2/C_{18}$-3.3.2-t | 9.5 | $1.7*10^{-2}$ ± 110 % |
| $Fe_3O_4/SiO_2$ $NH_2/C_{18}$-3.3.1-x | 32 | $3.2*10^{-2}$ ± 20 % |

The capacity of the particles after the first recycling decreased drastically. This could be due to the presence of contaminating compounds in the octane, which may have been attracted to the propylamine. And since the ratio of octane to propylamine is so large (100 mL to 60 µL), there was no propylamine left to clean the surface. The method for the recycling of the particles needs to be adjusted. Less octane and more propylamine could be used.

## 7. Conclusions

Commercial silica particles with known amino (-$NH_2$) group grafting degree were purchased and tested to confirm the amino groups selectivity towards NA in a real oil. FTIR, TAN, elemental analysis and asphaltene precipitation analysis were performed on the Heidrun crude oil before and after addition of the particles. It was observed that 29.6 % of possibly acidic asphaltenes were removed after particle treatment. The results also revealed a reduction of 92.2 % in TAN. No changes in concentrations of other crude oil components were observed.

The next step was to design our own nanoparticles capable of adsorbing HBA acid from a model solution. The $Fe_3O_4/SiO_2$ $NH_2/C_{18}$ nanoparticles were obtained through synthesis by two different methods including high-pressure autoclave experiment and reflux experiment using solvent of higher boiling point. The particles were tested with respect to various parameters and exhibited magnetic properties.

A specific surface area of 113 $m^2/g$ was measured for the $Fe_3O_4/SiO_2$ particles, while a slight reduction was registered for the functionalized samples, 86.9 $m^2/g$. and 94.2 $m^2/g$ for the particles modified in xylene and toluene respectively. Elemental analysis revealed that 3-aminopropyltrimethoxysilane (APTMS) groups had been successfully grafted onto the surface and n-octadecyltriethoxysilane (ODS) had been grafted to a far lesser degree or not at all. This may be because the amino groups on the APTMS molecule may be attracted to the silica surface, and when it is already adsorbed to the surface. It may be a higher probability for the APTMS molecule to graft onto the surface compared to the ODS molecule. The transmission electron microscopy allowed seeing the magnetic core and silica coating of the separate particles as well as particle agglomerates. The average particle size and coating thickness were calculated based on a size distribution analysis. The average size for the naked $Fe_3O_4$ particles was 10 nm, while thickness of the silica coating was estimated to be ca. 4.5 nm for the $Fe_3O_4/SiO_2$ particles.

The two functionalization methods revealed similar results for the adsorption of model NA (HBA) onto the particle surface. The amino-functionalized $Fe_3O_4/SiO_2$ $NH_2/C_{18}$ samples showed about 2.5 to 2.9 times higher adsorption capacity compared to the silica-coated $Fe_3O_4/SiO_2$ particles. Both functionalization methods showed similar results and can be used for successful modification of the magnetic silica-coated nanoparticles.

A procedure for cleaning and reusing the particles was developed and tested once. The conclusion was that the procedure needs to be improved as it did not seem to remove the adsorbed compounds.

As for the future work, it would be interesting to test the functionalized particles for the multiple extractions and develop effective recycling procedures. The adsorption has so far only been tested on a model system. Experiments on a real crude oil systems could give a better idea about possibly of application of such particles in actual industrial conditions.

# 8. References


1. Ronander, M., *Magnetic nanoparticles for extraction of naphthenic acids from crude oils,* 2015 Master thesis, NTNU.
2. Zhang, A., Ma, Q., Wang, K., Liu, X., Shuler, P., Tang, Y., *Naphthenic acid removal from crude oil through catalytic decarboxylation on magnesium oxide.* Applied Catalysis A: General, 2006. **303**: p. 103-109.
3. Lutnaes, B.F., Brandal, Ø., Sjöblom, J., Krane, J., *Archaeal C80 isoprenoid tetraacids responsible for naphthenate deposition in crude oil processing.* Organic and Biomolecular Chemistry, 2006. **4**(4): p. 616-620.
4. Williams, H., Dyer, S., Graham, G. M. . *Understanding the Factors Influencing the Formation and Control of Calcium Naphthenate Solids and Stabilised Emulsions Using a Novel Laboratory Flow Rig*. in *International Symposium on Oilfield Chemistry*. 2007. Houston, Texas, U.S.A.
5. Robbins, W.K., *Challenges in the characterization of naphthenic acids in petroleum.* Preprints/American Chemical Society, Division of Petroleum Chemistry, 1998. **42**(1): p. 137-140.
6. Brocart, B., Bourrel, M., Hurteven, C., Volle, J-L., and Escoffier, B., *ARN-Type Naphthenic Acids in Crudes: Analytical Detection and Physical Properties.* Journal of Dispersion Science and Technology, 2007. **28**: p. 331–337.
7. Rousseau, G., Zhou, H. & Hurtevent, C. *Calcium carbonate and naphthenate mixed scale in deep-offshore fields*. in *SPE Oilfield Scale Symposium.* 2001. Aberdeen, UK.
8. https://en.wikipedia.org/wiki/Flow_assurance.
9. Shepherd, A.G., Thimson, G. B., Westacott, R., Sorbie, K. S.,Heriot-Watt, U., Turner M., Smith, P. C. *Analysis of Organic Field Deposits: New Types of Calcium Naphthenate Scale of the Effect of Chemical Treatment?* in *SPE International OIlfield scale Symposium* 2006. Aberdeen, Scotland, U.K.
10. http://www.scaledsolutions.com/. 29.08.2016.
11. Oduola , L., Igwebueze, C. U., Smith, O., Vijn, P., Shepherd, A. G., *Calcium Naphthenate Solid Deposit Identification and Control in Offshore Nigerian Fields*, in *SPE International Symposium on Oilfield Chemistry*. 2013: The Woodlands, Texas, USA.
12. Samedov, A.M., Alieva, L.I. and Abbasov, V. M., *Inhibitive and Bactericidal Effects of Natural Naphthenates on Steel Corrosion in Sea Water.* Protection of Metals, 2008. **44**(4): p. 397–401.
13. Ubbels, S.J. *Preventing naphthenate stabilized emulsions and naphthenate deposits during crude oil processing.* in *5th international conference on petroleum phase behaviour and fouling*. 2004.
14. Rousseau, G., Zhou, H. & Hurtevent, C. . *Calcium carbonate and naphthenate mixed scale in deep-offshore fields*. in *SPE Oilfield Scale Symposium*. 2001. Aberdeen, UK.
15. Rodriguez, R.A., Ubbels, S. J., *Understanding naphthenate salt issues in oil production.* World Oil, 2007. **228**(8): p. 143-145.
16. Lu, A.-H.S., E.L.; Schuth, F., *Magnetic Nanoparticles: Synthesis, Protection, Functionalization, and Application.* Angewandte Chemie International Edition, 2007. **46**: p. 1222-1244.
17. Peng, D.L., Sumiyama, K., Hihara, T., Yamamuro, S., Konno, T.J., *Magnetic properties of monodispersed Co/CoO clusters.* Physical Review B, 2000. **61**(4): p. 3103.
18. Niemeyer, C.M., Mirkin, C. A., *Nanobiotechnology: Concepts, Applications and Perspectives*. 2006: John Wiley & Sons.

19. Wu, W., He, Q., Jiang, C., *Magnetic Iron Oxide Nanoparticles: Synthesis and Surface Functionalization Strategies.* Nanoscale Research Letters, 2008. **3**: p. 397–415.
20. Stöber, W., Fink, A., *Controlled growth of monodisperse silica spheres in the micron size range.* Journal of Colloid and Interface Science, 1968. **26**(1): p. 62–69.
21. Philipse, A.P., van Bruggen, M. P. B., Pathmamanoharan, C., *Magnetic silica dispersions: preparation and stability of surface-modified silica particles with a magnetic core.* Langmuir, 1994. **10**(1): p. 92–99.
22. Smith, J.E., Wang, L., Tan, W., *Bioconjugated silica-coated nanoparticles for bioseparation and bioanalysis.* TrAC Trends in Analytical Chemistry, 2006. **25**(9): p. 848–855.
23. Lu, Y., Yin, Y., Mayers, B. T., Xia, Y., *Modifying the Surface Properties of Superparamagnetic Iron Oxide Nanoparticles through A Sol−Gel Approach.* Nano Letters, 2002. **2**(3): p. 183–186.
24. Zhang, X., Niua, H., Pana, Y., Shia, Y., Cai, Y., *Modifying the surface of Fe3O4/SiO2 magnetic nanoparticles with C18/NH2 mixed group to get an efficient sorbent for anionic organic pollutants.* Journal of colloid and interface science, 2011. **362**(1): p. 107–112.
25. Yokoia, T., Kubotab, Y., Tatsumi, T., *Amino-functionalized mesoporous silica as base catalyst and adsorbent.* Applied Catalysis A: General, 2012. **421-422**: p. 14– 37.
26. Araghia, S.H., Entezari, M. H., *Amino-functionalized silica magnetite nanoparticles for thesimultaneous removal of pollutants from aqueous solution.* Applied Surface Science, 2015. **333**: p. 68-77.
27. Klein, L.C., *A review of: "Sol-Gel Science - The Physics and Chemistry of Sol-Gel Processing" Edited by C. Jeffrey Brinker and George W. Scherer.* Materials and Manufacturing Processes, 1994. **9**(5): p. 1007.
28. Kralj, S., Drofenik, M., Makovec, D., *Controlled surface functionalization of silica-coated magnetic nanoparticles with terminal amino and carboxyl groups.* Journal of Nanoparticle Research, 2011. **13**: p. 2829–2841.
29. Luechinger, M., Prins, R., Pirngruber, G. D., *Functionalization of silica surfaces with mixtures of 3-aminopropyl and methyl groups.* Microporous and Mesoporous Materials, 2005. **85**: p. 111–118.
30. De, D., Mandal, S., Bhattacharya. J., Ram, S., Roy, S., *Iron oxide nanoparticle-assisted arsenic removal from aqueous system.* Journal of environmental science and health. Part A, Toxic/hazardous substances & environmental engineering, 2009. **44**(2): p. 155–162.
31. Adedosu, T.A., Sonibare, O.O., *Characterization of Niger Delta Crude Oil by Infrared Spectroscopy.* Journal of applied sciences, 2005. **5**(5): p. 906-909.
32. Jackson, L.P. (2010) *EPA Should Clarify and Strengthen Its Waste Management Oversight Role With Respect to Oil Spills of National Significance*
33. Authority, A.M.S. (2009) *Identification of Oil on Water: Aerial Observation and Identification Guide*.
34. Barron, M.G., *Ecological Impacts of the Deepwater Horizon Oil Spill: Implications for Immunotoxicity.* Toxicologic Pathology, 2012. **40**: p. 315-320.
35. Pavıa-Sanders, A., Zhang, S., Flores, J. A., Sanders, J. E., Raymond, J. E., and Wooley, K.L. , *Robust magnetic/polymer hybrid nanoparticles designed for crude oil entrapment and recovery in aqueous environments.* ACS Nano, 2013. **7**(9): p. 7552-61.
36. Atta, A.M., Al-Lohedan, H. A., and Al-Hussain, S. A., *Functionalization of magnetite nanoparticles as oil spill collector.* International Journal of Molecular Sciences, 2015. **16**(4): p. 6911-31.

37. Yu, L., Hao, G., Liang, Q., and Jiang, W., *Fabrication of Magnetic Porous Silica Submicroparticles for Oil Removal from Water.* Industrial & Engineering Chemistry Research, 2015. **54**(38): p. 9440–9449.
38. Stanford, L.A., Rodgers, R. P., Marshall, A. G. , *Compositional Characterization of Bitumen/ Water Emulsion Films by Negative- and Positive-Ion Electrospray Ionization and Field Desorption/Ionization Fourier Transform Ion Cyclotron Resonance Mass Spectrometry.* Energy Fuels 2007. **21**: p. 963−972.
39. Rondón, M., Pereira, J. C., Bouriat, P., Graciaa, A., Lachaise, J., Salager, J. L. , *Breaking of water-in-crude-oil emulsions. 2. Influence of asphaltene concentration and diluent nature on demulsifier action.* Energy and Fuels, 2008. **22**(2): p. 702–707.
40. Ese, M.-H., Yang, X. and Sjoblom, J., *Film Forming Properties of Asphaltenes and Resins. A Comparative Langmuir-Blodgett Study of Crude Oils from North Sea, European Continent and Venezuela.* Colloid and Polymer Science, 1998. **276**: p. 800-809.
41. Cunha, R.E.P., Fortuny, M., Dariva, C., Santos, A. , *Mathematical Modeling of the Destabilization of Crude Oil Emulsions Using Population Balance Equation.* Industrial & Engineering Chemistry Research, 2008. **47**: p. 7094−7103.
42. Peng, J., Liu, Q., Xu, Z., and Masliyah, J., *Synthesis of Interfacially Active and Magnetically Responsive Nanoparticles for Multiphase Separation Applications.* Advanced Functional Materials 2012. **22**(8): p. 1732–1740.
43. Ali, N., Zhang, B., Zhang, H., Zaman, W., Li, X., Li, W., Zhang, Q., *Interfacially active and magnetically responsive compositenanoparticles with raspberry like structure; synthesis and itsapplications for heavy crude oil/water separation.* Colloids and Surfaces A: Physicochemical and Engineering Aspects, 2015. **472**: p. 38–49.
44. Liang, J., Du, N., Song, S., Hou, W., *Magnetic demulsification of diluted crude oil-in-waternanoemulsions using oleic acid-coated magnetite nanoparticles.* Colloids and Surfaces A: Physicochemical and Engineering Aspects, 2015. **466**: p. 197–202.
45. Prigiobbe, V., Ko, K., Wang, Q., Huh, C., Bryant, S. L., Bennetzen, M. V. *Magnetic Nanoparticles for Efficient Removal of Oilfield "Contaminants": Modeling of Magnetic Separation and Validation*. in *SPE International Symposium on Oilfield Chemistry*. 2015. The Woodlands, Texas, USA.
46. Ko, S., Prigiobbe, V., Huh, C., Bryant, S. L., Bennetzen, M. V., Mogensen, K. *Accelerated Oil Droplet Separation from Produced Water Using Magnetic Nanoparticles*. in *SPE Annual Technical Conference and Exhibition*. 2014. Amsterdam, The Netherlands.
47. Rahmani, A.R., Bryant, S. L., Huh, C., Ahmadian, M., Zhang, W., Liu, Q. H. *Characterizing Reservoir Heterogeneities Using Magnetic Nanoparticles*. in *SPE Reservoir Simulation Symposium*. 2015. Houston, Texas, USA.
48. Oliveira, G.E., Clarindo, J. E. S., Santo, K. S. E., Souza Jr., F. G., *Chemical Modification of Cobalt Ferrite Nanoparticles with Possible Application as Asphaltene Flocculant Agent.* Materials Research, 2013. **16**(3).
49. Maity, S.K., Anchieyta, J., Soberanis, L., and Alonso F., *Catalysts for Hydroprocessing of Maya Heavy Crude.* Applied Catalysis A: General 2003. **253**: p. 125-134.
50. Haindade, z.M.W., Bihani, A. D., Javeri, S. M., Jere, C. B. *Enhancing Flow Assurance Using Co-Ni Nanoparticles For Dewaxing Of Production Tubing*. in *SPE International Oilfield Nanotechnology Conference and Exhibition*. 2012. Noordwijk, The Netherlands.
51. Mehta, P., Huh, C., Bryant, S. L. *Evaluation of superparamagnetic nanoparticle-based heating for flow assurance in subsea flowlines*. in *International Petroleum Technology Conference*. 2014. Kuala Lumpur, Malaysia.

52. Soares, F.S.-M., de A., Prodanovic, M., Huh, C. *Excitable Nanoparticles for Trapped Oil Mobilization*. in *SPE Improved Oil Recovery Symposium*. 2014. Tulsa, Oklahoma, USA.
53. D664-95 ASTM method: Standard Test Method for Acid Number of Petroleum Products by Potentiometric Titration
54. Mullins, O., Sheu, Eric Y. *Structures and Dynamics of Asphaltenes.* Springer 1998.
55. Blaney, Lee, *"Magnetite (Fe3O4): Properties, Synthesis, and Applications"*. Volume 15 - 2007. Paper 5.
56. Zhuravlev, L.T., *The surface chemistry of amourphous silica. Zhuralev model.* Colloids and Surfaces A: Physiochemical and Engineering Aspects 2000. **173**: p. 1-38
57. http://www.mindat.org/min-2538.html. 29.08.2016.
58. http://www.chemspider.com/Chemical-Structure.148691.html. 29.08.2016.

# 9. Appendices

## 9.1. Instruments

All instruments are listed by production company and model.

*Hardware:*

| **Production company** | **Model** |
|---|---|
| Amazing magnets | D500P, size: 2” × 0.5” Grade: N40 |
| Eppendorf | Centrifuge 5810 |
| Micrometics Instrument Corporation | TriStar 3000 Gas Adsorption Analyzer |
| JEOL | NORTEM JEOL JEM-2100F Electron Microscope |
| Bruker Optics | IR Spectrophotometer Tensor 27 |
| Shimadzu | UV-2401PC, UV-vis Recording Spectrophotometer |
| Hellma Analytics | Precision cells made of Quartz Suprasil ® |
| IKA | HS 501 digital Laboratory shaker |
| KSV Instruments Ltd | KSV QCM-Z500 Microbalance |

*Software:*

| **Production company** | **Name and version** |
|---|---|
| Bruker | OPUS software |
| Shimadzu | UVProbe 2.10 |
| Micromeritics Instrument Corporation | Tristar 300 software Version 6.04 |
| Gatan Microscpy Suite | DigitalMicrograph Version 2.32.888.0 |

## 9.2. Figures

The calibration curves of Heidrun crude oil at 224 nm and 212nm are given in Figure A.1.

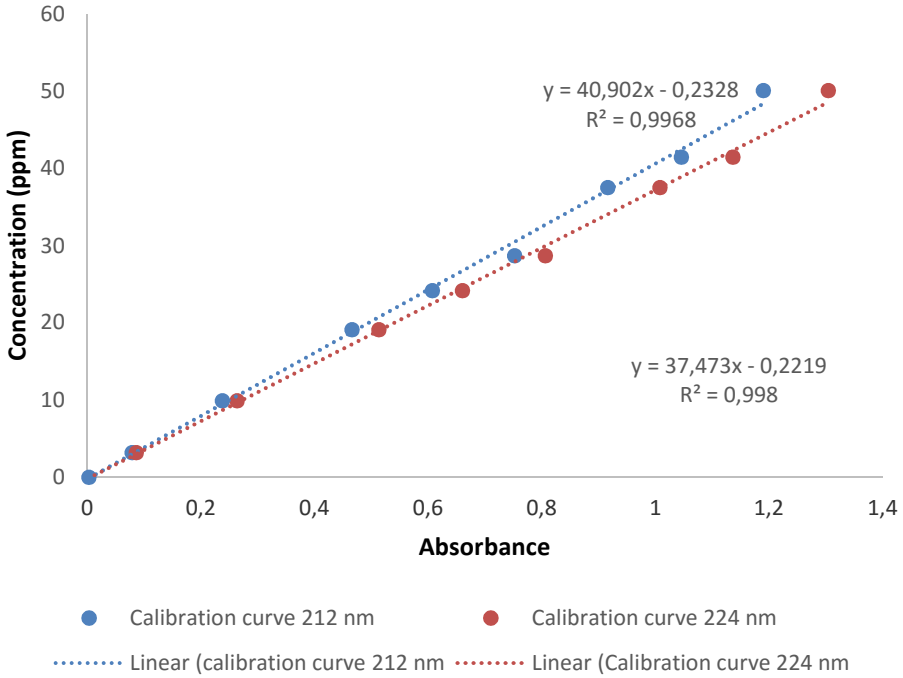


***Figure A.1:*** *Calibration curves of Heidrun crude oil in toluene.*

Calibration curve for HBA in octane is given in Figure A.2.

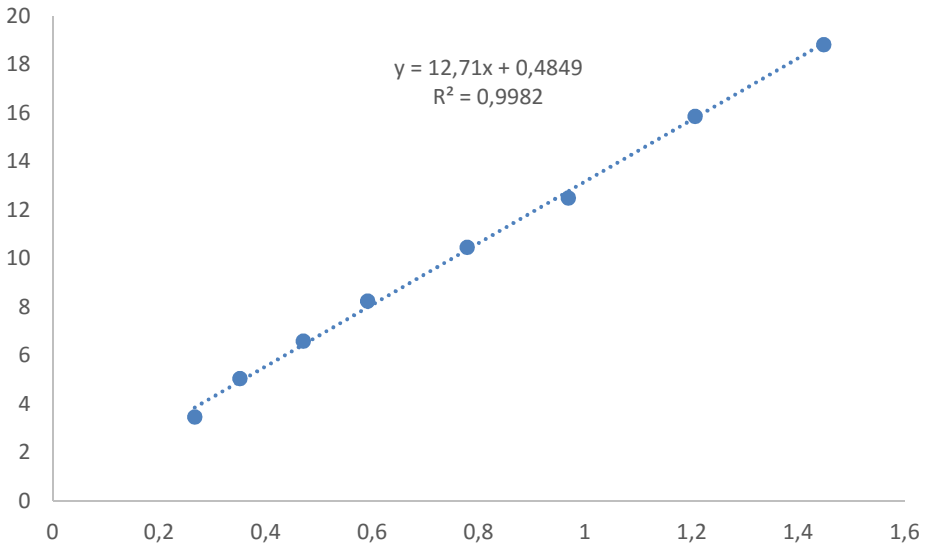


***Figure A.2:*** *Calibration curve for 4-heptyl benzoic acid in octane.*

Figure A.3 and A.4 give the size measurements of distinguishable particles. The measurements were taken horizontally and at the particle's thickest point.

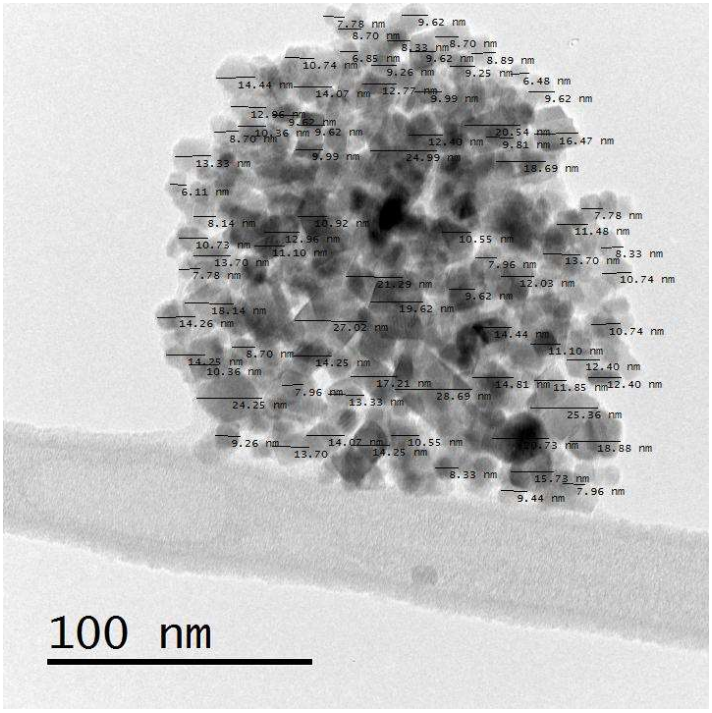


***Figure A.3:*** *Size distribution of $Fe_3O_4$ particles, the measurement were taken horizontally to the picture and at thickest place.*

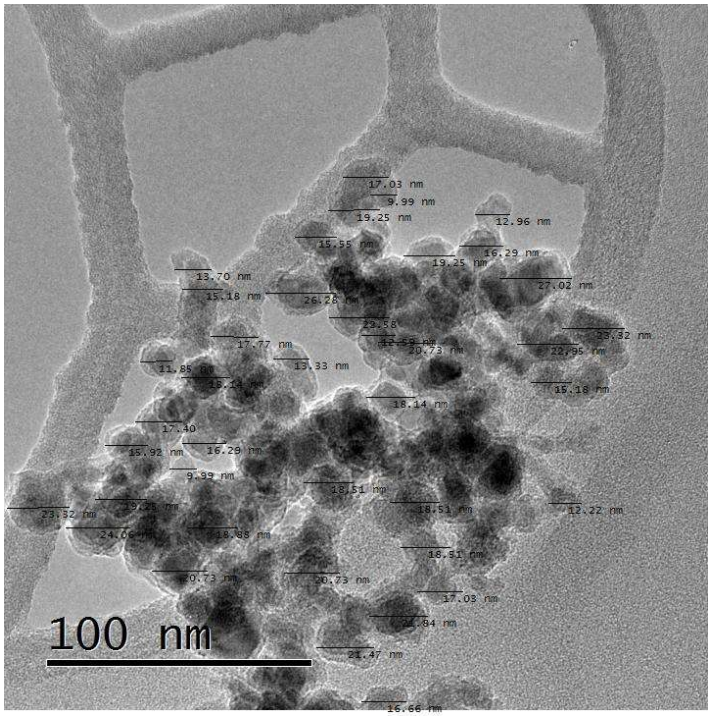


***Figure A.4:*** *Size distribution of $Fe_3O_4/SiO_2$-3.3, the measurement were taken horizontally to the picture and at thickest place.*

In Figure A.5 lattice spacing value measurements are shown.

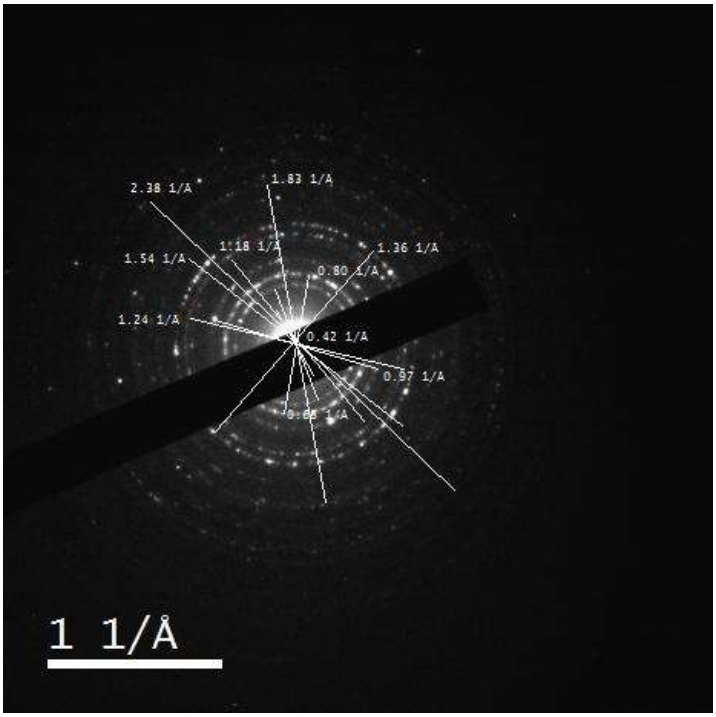


***Figure A.5:*** *Lattice measurement from driffaction image of $Fe_3O_4$-3.*

Figure A.6 shows XRD analysis of $Fe_3O_4$ particles from Ronander's Master's thesis [1]. The 2θ values are given in Table A.6.

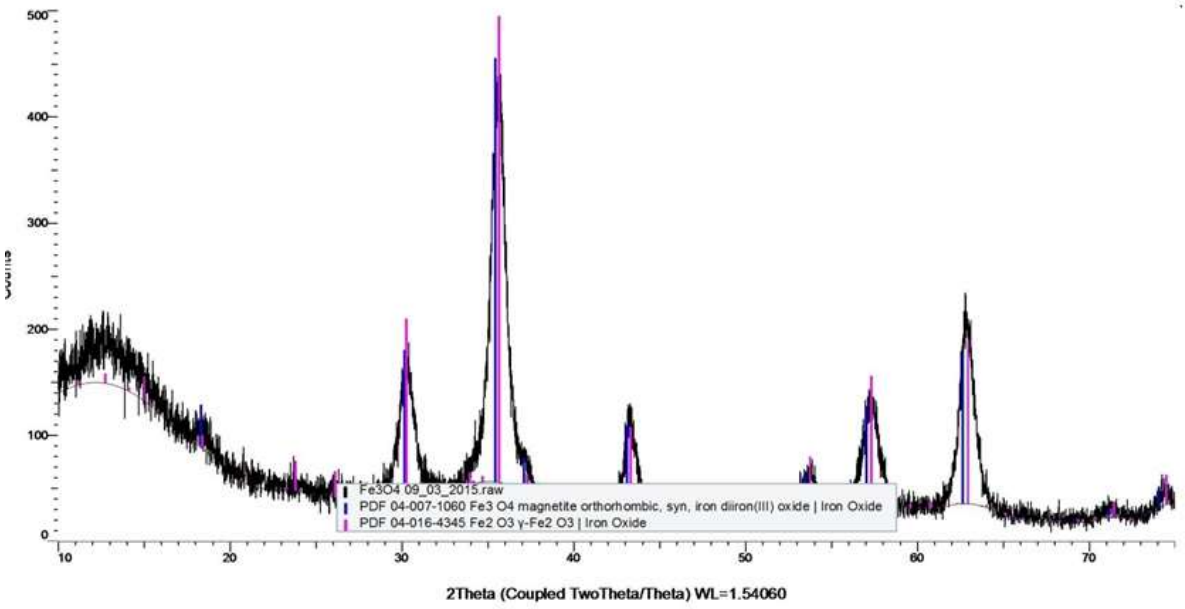


***Figure A.6:*** *X-Ray diffractogram from Mia Ronander's Master's thesis[1].*

## 9.3. Tables

Equation A.1 gives the concentration of titrant. The measured values are given in Table A.1.

$$C = \frac{m_{BA}}{M_{BA} V_{eq}} \tag{A.1}$$

where $C$ is the concentration of TBA, $m_{BA}$ is the mass of benzoic acid, $M_{BA}$ is the molecular weight of benzoic acid and $V_{eq}$ is the volume of titrant at infliction point.

***Table A.1**: Concentration determination of TBA.*

| Parallel | Volume titrant (mL) | Mass benzoic acid (mg) | Concentration TBA (M) |
|---|---|---|---|
| 1 | 5.83 | 65.5 | $9.21*10^{-2}$ |
| 2 | 5.20 | 58.4 | $9.19*10^{-2}$ |

$M_{BA}$=122.12 g/mol. Table A.1 gives an average concentration of $9.20*10^{-2}$ M with a standard deviation from average of $4.47*10^{-5}$

The equilibrium concentrations are presented in Tables A.2 and A.3 UV-vis measurements. The surface concentration is calculated from the equation 5.1.

***Table A.2:** Surface concentration sample points for FMN in toluene, $C_e$ is equilibrium concentration and $\Delta C$ is the difference between start concentration and $C_e$.*

| Sample | $C_e$ ($g_{HBA}$/L) | $\Delta C$($g_{HBA}$/L) | Surface concentration (mg/m$^2$) |
|---|---|---|---|
| 1 | 0.001 | 0.098 | 0.162 |
| 2 | 0.014 | 0.331 | 0.518 |
| 3 | 0.058 | 0.429 | 0.740 |
| 4 | 0.235 | 0.457 | 0.770 |
| 5 | 0.505 | 0.482 | 0.814 |
| 6 | 0.875 | 0.359 | 0.745 |
| 7 | 1.480 | 0.497 | 0.760 |
| 8 | 1.987 | 0.481 | 0.779 |

***Table A.3:*** *Surface concentration sample points for FMN in xylene, $C_e$ is equilibrium concentration and ΔC is the difference between start concentration and $C_e$.*

| Sample | $C_e$ ($g_{HBA}$/L) | ΔC($g_{HBA}$/L) | Surface concentration (mg/m$^2$) |
|---|---|---|---|
| 1 | 0.001 | 0.097 | 0.175 |
| 2 | 0.004 | 0.338 | 0.581 |
| 3 | 0.056 | 0.422 | 0.760 |
| 4 | 0.220 | 0.468 | 0.810 |
| 5 | 0.498 | 0.493 | 0.844 |
| 6 | 1.007 | 0.475 | 0.870 |
| 7 | 1.515 | 0.478 | 0.829 |
| 8 | 1.976 | 0.491 | 0.872 |

The surface in Table A.4 was calculated using the specific surface area of $Fe_3O_4/SiO_2$-3.3.1-x, 86.9 m$^2$/g (Chapter 6.2.4). The surface in the Table A.5 was calculated using the specific surface area of $Fe_3O_4/SiO_2$-3.3.2-t, 94.2 m$^2$/g (Chapter 6.2.4). The volume in the Tables A.4 and A.5 was calculated using a density 0.703 kg/L for octane and assuming that the increase of density in the stock solution is negligible.

***Table A.4:*** *Measured concentration of HBA in octane for adsorption experiment of FMN from xylene. The concentration was prepared from a stock solution (2.468 g/L).*

| Sample | FMN (mg) | Surface (m$^2$) | Octane (g) | Stock (g) | $C_0$ ($g_{HBA/L}$) | V (mL) |
|---|---|---|---|---|---|---|
| 1 | 32.1 | 2.77 | 3.3930 | 0.1402 | 0.098 | 5.026 |
| 2 | 33.6 | 2.92 | 3.0158 | 0.4861 | 0.343 | 4.981 |
| 3 | 31.9 | 2.77 | 2.8341 | 0.6714 | 0.477 | 4.998 |
| 4 | 33.1 | 2.88 | 2.5206 | 0.9759 | 0.689 | 4.974 |
| 5 | 33.7 | 2.93 | 2.1106 | 1.4160 | 0.991 | 5.017 |
| 6 | 31.3 | 2.88 | 1.3980 | 2.1023 | 1.482 | 4.979 |
| 7 | 32.9 | 2.86 | 0.6714 | 2.8172 | 1.515 | 4.962 |
| 8 | 32.5 | 2.82 | 0 | 3.5187 | 2.468 | 5.005 |

***Table A.5:*** *Measured concentration of HBA for adsorption experiment of FMN from toluene. The concentration was prepared from a stock solution (2.468 g/L).*

| Sample | FMN (mg) | Surface ($m^2$) | Octane (g) | Stock (g) | $C_0$ ($g_{HBA/L}$) | V (mL) |
|---|---|---|---|---|---|---|
| 1 | 32.0 | 3.014 | 3.3537 | 0.1402 | 0.099 | 4.970 |
| 2 | 34.0 | 3.202 | 3.0190 | 0.4923 | 0.346 | 4.995 |
| 3 | 30.5 | 2.873 | 2.7964 | 0.6870 | 0.487 | 4.955 |
| 4 | 31.4 | 2.957 | 2.5179 | 0.9819 | 0.692 | 4.978 |
| 5 | 31.3 | 2.948 | 2.1031 | 1.4004 | 0.986 | 4.984 |
| 6 | 30.6 | 2.882 | 2.1021 | 2.1032 | 1.234 | 5.982 |
| 7 | 35.1 | 3.306 | 0.7036 | 2.8358 | 1.977 | 5.035 |
| 8 | 33.0 | 3.108 | 0 | 3.5355 | 2.468 | 5.029 |

Lattice spacing values, calculated using Braggs law (6.16) with λ= 1.5406 Å, and 2θ values from Figure A.6 are given in Table A.6.

***Table 6.A:*** *2θ and lattice spacing values from Ronander's Master's thesis [1].*

| 2θ values at peaks | Lattice spacing (Å) |
|---|---|
| 30.0 | 2.98 |
| 35.5 | 2.53 |
| 43.3 | 2.09 |
| 53.8 | 1.70 |
| 57.2 | 1.61 |
| 62.8 | 1.48 |
| 74.5 | 1.27 |